HHS Public Access

Author manuscript

Int J Pharm. Author manuscript; available in PMC 2024 January 02.

Published in final edited form as:

Int J Pharm. 2023 January 25; 631: 122502. doi:10.1016/j.ijpharm.2022.122502.

Semi-mechanistic reduced order model of pharmaceutical tablet dissolution for enabling Industry 4.0 manufacturing systems

Shumaiya Ferdoush[a], **Marcial Gonzalez**[a,b,*]

[a]School of Mechanical Engineering, Purdue University, West Lafayette, IN 47907, USA

[b]Ray W. Herrick Laboratories, Purdue University, West Lafayette, IN 47907, USA

Abstract

We propose a generalization of the Weibull dissolution model, referred to as *generalized Weibull dissolution model*, that seamlessly captures all three fractional dissolution rates experimentally observed in pharmaceutical solid tablets, namely decreasing, increasing, and non-monotonic rates. This is in contrast to traditional reduced order models, which capture at most two fractional dissolution rates and, thus, are not suitable for a wide range of product formulations hindering, for example, the adoption of knowledge management in the context of Industry 4.0. We extend the generalized Weibull dissolution model further to capture the relationship between critical process parameters (CPPs), critical materials attributes (CMAs), and dissolution profile to, in turn, facilitate real-time release testing (RTRT) and quality-by-control (QbC) strategies. Specifically, we endow the model with multivariate rational polynomials that interpolate the mechanistic limiting behavior of tablet dissolution as CPPs and CMAs approach certain values of physical significance (such as the upper and lower bounds of tablet porosity or lubrication conditions), thus the semi-mechanistic nature of the reduced order model. Restricting attention to direct compaction and using various case studies from the literature, we demonstrate the versatility and the capability of the semi-mechanistic ROM to estimate changes in dissolution due to process disturbances in tablet weight, porosity, lubrication conditions (i.e., the total amount of shear strain imparted during blending), and moisture content in the powder blend. In all of the cases considered in this work, the estimations of the model are in remarkable agreement with experimental data.

Keywords

Continuous manufacturing; Reduced order model; Dissolution prediction; Compacted tablets; Real-time release testing; Industry 4.0

[*]Corresponding author at: School of Mechanical Engineering, Purdue University, West Lafayette, IN 47907, USA. marcial-gonzalez@purdue.edu (M. Gonzalez).

CRediT authorship contribution statement

Shumaiya Ferdoush: Conceptualization, Methodology, Software, Validation, Formal analysis, Investigation, Data curation, Writing – original draft, Visualization. **Marcial Gonzalez:** Conceptualization, Methodology, Validation, Resources, Writing – review & editing, Supervision, Project administration, Funding acquisition.

Declaration of competing interest

The authors declare that they have no known competing financial interests or personal relationships that could have appeared to influence the work reported in this paper.

1. Introduction

Continuous manufacturing of pharmaceutical solid dosage forms offers potential flexibility, higher product quality, reduced manufacturing footprint, and economic advantages over batch manufacturing, in both product development and product manufacturing stages (Lee et al., 2015). However, while innovator companies are selectively adopting continuous manufacturing, the overwhelming majority of pharmaceutical plants employ batch operations. It is evident that even though continuous manufacturing offers notable benefits, it is not a universal solution. For example, batch production is sometimes cost-effective in terms of set-up cost. Similarly, continuous production is sometimes not feasible if unit operations have very different processing times, such as the period of tablet relaxation required before coating (Leane et al., 2018). In contrast, a recent U.S. Food and Drug Administration (FDA) audit indicates that continuous manufacturing applications have received faster regulatory approval and, in turn, made more revenues due to faster market entry compared to batch applications (Fisher et al., 2022). The adoption of continuous manufacturing has hastened the development of modern process systems engineering tools, such as process modeling, online process analytical technology (PAT), active process control, material tracking, and real-time risk assessment, among others (Lee et al., 2015; Lakerveld et al., 2013; Byrn et al., 2015; Gao et al., 2011; Kvarnström and Bergquist, 2012). These developments certainly lead to enhanced product knowledge and process understanding which, ultimately, provide a platform for realizing quality-by-design (QbD) (Yu, 2008) and real-time release testing (RTRT) (Markl et al., 2020) and, eventually, for ensuring consistent product quality based on process data (Chatterjee, 2012).

The FDA has released guidelines for implementing QbD in the pharmaceutical manufacturing process (FDA and CDER, 2006). The QbD framework emphasizes the use of systematic approaches to process development for new drug products, which utilize enhanced process and product understanding based on sound scientific principles. Once the critical quality attributes (CQAs) of the pharmaceutical product have been identified, mechanistic and data-driven mathematical models can be used to deduce how critical process parameters (CPPs) and critical material attributes (CMAs) affect the CQAs and, in turn, to identify the design space (DS) where the process can be operated so that the target product profile (TPP) is not affected due to changes in operating conditions (Lawrence et al., 2014). The QbD framework can be extended to a quality-by-control (QbC) framework (Su et al., 2019b) through active process control strategies to handle, for example, operating problems related to process disturbances and uncertainties in real-time. Evidently, the development of mechanistic and semi-mechanistic reduced order models (ROMs), resulting from a trade-off between complexity and performances but still based on product and process understanding, forms an essential cornerstone for process design, optimization, and control in pharmaceutical manufacturing.

The dissolution profile is one of the most important CQAs for any pharmaceutical solid dosage form (Lawrence et al., 2014). Dissolution tests are time-consuming destructive tests that are used as surrogates for in-vivo drug release and the bioavailability of drugs. They are performed offline to ensure batch-to-batch manufacturing consistency and, for example, evaluate post-approval formulation changes to product quality (FDA and CDER, 1997).

Therefore, predictive dissolution ROMs are crucial for the successful implementation of any RTRT strategy (FDA, 2004, 2012; Wu et al., 2015). In the context of continuous manufacturing, these models must generate a dissolution profile based on prior product knowledge and process understanding, CPPs monitored in real-time, and any in-line and at-line PAT available (Zaborenko et al., 2019). By way of example, Fig. 1 shows the Continuous Solids Processing Pilot Plant at Purdue University. The API and excipients are fed through K-Tron and Schenck feeders, respectively, and uniformly blended in a Gericke GCM-250 blender. Depending on the manufacturing process, namely direct compaction or dry granulation, the powder blend is next sent to a K-Tron MT12 micro-screw lubricant feeder or an Alexanderwerk WP120 roller compactor for dry granulation. Finally, solid tablets are produced by a Natoli NP-400 rotary tablet press. Among many other CPPs and CMAs, we identified the following dominant CPPs and CMAs that affect the dissolution of a solid oral dosage form: (i) API concentration (Pawar et al., 2016b; Wenzel et al., 2017), (ii) crystal size distribution (Chu et al., 2012; Nagy et al., 2021), (iii) lubrication (lubricant concentration (Uzunović and Vranić, 2007) and shear strain Hernandez et al. (2016), Pingali et al. (2011)), (iv) glidant (Pingali et al., 2011) (v) moisture content in powder blend (Steendam et al., 2000, 2001), (vi) compaction force (Pingali et al., 2011; Pawar et al., 2016b), and (vii) tablet porosity (Hattori and Otsuka, 2011).

Drug dissolution is classically considered to be governed by the Noyes–Whitney equation (Noyes and Whitney, 1897), namely the dissolution rate is proportional to the difference of dissolved drug concentration C at time t from the solubility level C_s, i.e., $\dot{C}(t) \propto [C_s - C(t)]$. Similarly, Lánsky and Weiss (2001) proposed that the mass of drug dissolved from a pharmaceutical solid product $M(t)$ can be empirically described by

$$\dot{M}(t) = K(t)[M_\infty - M(t)] \tag{1}$$

where M_∞ is the dose of the solid product, i.e., the total mass of API in the solid product, and $K(t)$ is the fractional dissolution rate, i.e., the ratio of dissolution rate to the undissolved amount. For a homogeneous compound and well-stirred dissolution medium (Lánsky and Weiss, 1999), the fractional dissolution rate is assumed constant in time and, in turn, the classical first-order model is recovered. In general, the fractional dissolution rate $K(t)$ can be interpreted as the conditional probability that a randomly selected API molecule transfers from the solid state into the solution during a differential period of time, given that the dissolution has not taken place before time t. There is a large spectrum of mechanistic and empirical models for characterizing drug release profiles (see, e.g., Bruschi (2015), Costa and Lobo (2001) and references therein), that either has the form of or can be interpreted as an approximation of Eq. (1) over a short period of time. A ROM of pharmaceutical tablet dissolution for realizing QbD and QbC frameworks, however, needs to predict changes in dissolution profile both due to process disturbances, for process control purposes, and over a wide design space, for process design and optimization purposes. Furthermore, a dissolution model suitable for a wide range of product formulations is desirable, since it facilitates knowledge management in the context of Industry 4.0 (Ding, 2018). In this work, we will establish that there is a lack of a dissolution ROM with such general behavior, and we will present a generalization of the Weibull dissolution model (Costa and Lobo, 2001) which

overcomes this limitation. Furthermore, a ROM suitable for QbD and QbC frameworks needs to relate the dissolution profile with CPPs and CMAs of the manufacturing process. In this work, we restrict attention to direct compaction (i.e., manufacturing route (A) in Fig. 1) and we illustrate this concept by extending the generalized Weibull dissolution model to process disturbances in tablet porosity, lubrication conditions (i.e., the total amount of shear strain imparted during blending), and moisture content in the powder blend.

The paper is organized as follows. In Section 2, a generalized Weibull dissolution model is proposed and its equivalence to classical dissolution models is established. The performance of the proposed model is demonstrated in Section 3 using selected experimental data from published dissolution tests of pharmaceutical formulations. The model is extended to capture the relationship between CPPs, CMAs, and the dissolution profile of solid tablets, and the resulting semi-mechanistic reduced order dissolution model for continuous manufacturing is presented in Section 4. A parameter identification method that maximizes the similarity factor between dissolution experimental data and model predictions is presented in the same section. The versatility and capability of the semi-mechanistic ROM to estimate changes in dissolution due to process disturbances are demonstrated in Section 5 using various case studies from the literature. The formulation, fabrication, and characterization of lomustine tablets (an oral antineoplastic agent for the treatment of primary and metastatic brain tumors) are discussed in Section 6. The model parameter estimation of a lomustine tableting-dissolution ROM and the applicability of this model to RTRT in continuous manufacturing are examined in the same section. Possible avenues for extending this line of work is described in Section 7. Concluding remarks are presented in Section 8.

2. A generalized Weibull dissolution model

Lánsky and Weiss (2003) established that the fractional dissolution rate can be classified into three types, namely decreasing fractional dissolution rate (DFR), increasing fractional dissolution rate (IFR), and non-monotonic fractional dissolution rate (NMFR). Fig. 2 illustrates that apparently similar dissolution profiles can have distinctively dissimilar fractional dissolution rate profiles. A time-dependent fractional dissolution rate is influenced by the heterogeneity of the dissolving tablet, e.g., by the polydispersity of the API crystals, and, hence, it is prevalent in pharmaceutical solid products. In fact, all three fractional dissolution rate profiles are observed in commercial products. Similarly, mechanistic and empirical models typically used to characterize drug release profiles (see, e.g., Bruschi (2015), Costa and Lobo (2001) and references therein) exhibit at least one of these fractional dissolution rate profiles. For example, Macheras and Dokoumetzidis (2000) showed that the fractional dissolution rate of the Weibull dissolution model is a power function of time. As we established before, in the context of Industry 4.0, it is desirable to adopt a dissolution model suitable for a wide range of process states and product formulations to, e.g., realize QbD and QbC frameworks and facilitate knowledge management. In this section, we will establish that there is a lack of a dissolution ROM with such general behavior, and we will propose a generalization of the Weibull dissolution model (Costa and Lobo, 2001) which overcomes this limitation.

The Weibull model is one of the most popular dissolution models in capturing the trend of experimental dissolution curves. It is characterized by the following time-dependent fractional dissolution rate

$$K(t) = \frac{kt^{k-1}}{\lambda^k} \text{ for } k > 0 \text{ and } t \in [0, \infty) \tag{2}$$

where λ and k are model parameters. Using definition (1), the fraction of drug released is given by

$$\frac{M(t)}{M_\infty} = 1 - e^{-(t/\lambda)^k} \text{ for } k > 0 \text{ and } t \in [0, \infty) \tag{3}$$

For $k > 1$, the fractional dissolution rate is of increasing type; for $k \in (0,1)$, the fractional dissolution rate is of decreasing type; for $k = 1$, the fractional dissolution rate is time-independent. The Weibull dissolution model does not capture a non-monotonic fractional dissolution trend (Lánsky and Weiss, 2003).

The zero-order dissolution model has the following fractional dissolution rate

$$K(t) = \begin{cases} 1/(a-t) & \text{for } t \in [0, a) \\ 0 & \text{for } t \in [a, \infty) \end{cases} \tag{4}$$

where a is a model parameter (Lánsky and Weiss, 2003). Using definition (1), the fraction of drug released is given by

$$\frac{M(t)}{M_\infty} = \begin{cases} t/a & \text{for } t \in [0, a) \\ 1 & \text{for } t \in [a, \infty) \end{cases} \tag{5}$$

The fractional dissolution rate increases before the dose is completely released at $t = a$, i.e., it increases before $M(a) = M_\infty$. Similarly, there is a family of classical models which have a time-dependent fractional dissolution rate over a finite interval of time only, and a fraction of drug released given by

$$\frac{M(t)}{M_\infty} = \begin{cases} 1 - (1 - t/a)^n & \text{for } t \in [0, a) \\ 1 & \text{for } t \in [a, \infty) \end{cases} \tag{6}$$

where a and n are model parameters (Wang and Flanagan, 1999; De Almeida et al., 1997). Furthermore, for $n = 3$, the model is known as the cube-root model or Hixson–Crowell model; for $n = 2$, the model is known as the square-root model; and for $n = 3/2$, the model is known as the three-half-root model. Evidently, the zero-order model is recovered for $n = 1$. The Hopfenberg model (Bruschi, 2015) specifically considers $a = C_0 a_0 / k_0$, where k_0 is the erosion grade constant, C_0 is the initial concentration of the drug in the matrix and a_0 is the initial characteristic size of the solid product — that is the radius of a sphere ($n = 3$) and cylinder ($n = 2$) or thickness of a film ($n = 1$). Using definition (1), the fractional dissolution rate is given by

$$K(t) = \begin{cases} n/(a-t) & \text{for } t \in [0, a) \\ 0 & \text{for } t \in [a, \infty) \end{cases} \tag{7}$$

and it increases for $t \in [0, a$. The Korsmeyer–Peppas models (Korsmeyer et al., 1983) also estimate that the dose is completely released over a finite interval of time, and they have a fraction of drug released given by

$$\frac{M(t)}{M_\infty} = \begin{cases} t^n/a & \text{for } t \in \left[0, a^{1/n}\right) \\ 1 & \text{for } t \in \left[a^{1/n}, \infty\right) \end{cases} \tag{8}$$

where a and n are model parameters. These models estimate that $M\left(a^{1/n}\right) = M_\infty$ and they are known for capturing only the first 60% of experimental trends (Korsmeyer et al., 1983). For $n = 1/2$, the model is known as Higuchi model; for $1/2 < n < 1$, the model is denoted as anomalous transport; for $n = 1$, the zero-order model is recovered; and for $n > 1$ the model is called Super Case-II transport. Using definition (1), the fractional dissolution rate of the Korsmeyer–Peppas model is given by

$$K(t) = \begin{cases} nt^{n-1}/(a-t^n) & \text{for } t \in \left[0, a^{1/n}\right) \\ 0 & \text{for } t \in \left[a^{1/n}, \infty\right) \end{cases} \tag{9}$$

Interestingly, these models belong to the increasing fractional dissolution rate class for $n \geq 1$ and to the non-monotonic class, otherwise. Similarly, the Peppas-Sahlin model can be expressed as (Peppas and Sahlin, 1989)

$$\frac{M(t)}{M_\infty} = C_1 t^m + C_2 t^{2m} \quad t \in \left[0, \min\left\{t_1^*, t_2^*\right\}\right) \tag{10}$$

where the first term is interpreted as the Fickian diffusional contribution, whereas the second term is the Case II relaxational contribution. In the above equation, $C_1 > 0$, $t_1^* = \left[\left(\sqrt{C_1^2 + 4C_2} - C_1\right)/2C_2\right]^{1/m}$ is the time at which the function reaches 1, and $t_2^* = \left[-C_1/2C_2\right]^{1/m}$ is the time at which the function reaches its maximum. Using definition (1), the fractional dissolution rate of the Peppas-Sahlin model is given by

$$K(t) = \frac{mC_1 t^{m-1} + 2mC_2 t^{2m-1}}{1 - C_1 t^m - C_2 t^{2m}} \quad t \in \left[0, \min\left\{t_1^*, t_2^*\right\}\right) \tag{11}$$

Interestingly, these models belong to the decreasing fractional dissolution rate class for $0 < m \leq 1$ and, otherwise, to the non-monotonic class. However, to the best of our knowledge, there is no dissolution ROM with all three fractional dissolution rate profiles.

We address this technical need by proposing a generalization of the Weibull model, referred to as *generalized Weibull dissolution model*. This new model has the following fractional dissolution rate and the fraction of drug released functions

$$K(t) = \frac{kt^{k-1}}{\lambda^k\left[1+(t/s)^k\right]} \text{ for } t \in [0,\infty) \tag{12}$$

$$\frac{M(t)}{M_\infty} = 1 - \left[1+(t/s)^k\right]^{-(s/\lambda)^k} \quad \text{for } t \in [0,\infty) \tag{13}$$

where λ, k and s are model parameters. In the limit of $s \to \infty$, the generalized Weibull model reduces to the Weibull model, that is to (2)–(3), and λ to the time interval necessary to release 63.2% of the dose. The parameter k is known as the shape parameter and, together with s, controls the type of fractional dissolution rate. For $0 < k \leq 1$, the fractional dissolution rate is of decreasing type for any value of s (see Fig. 3(a)). For $k > 1$, the maximum fractional dissolution rate occurs at time equal to $s(k-1)^{1/k}$ and, hence, the fraction dissolution rate profile is controlled by s (see Figs. 3(b) and 3(c)). Specifically, in the limit of $s \to \infty$, the fractional dissolution rate profile is increasing, and it is non-monotonic, otherwise.

We will demonstrate next that classical dissolution models are equivalent to the proposed generalized Weibull dissolution model in the initial stages of dissolution, that is they are equal to a number of terms in the Taylor expansion of the generalized Weibull model, or rather exactly equivalent, for certain values of λ, k, and s. Specifically, the Weibull model is exactly recovered in the limit of $s \to \infty$, as we established above, that is

$$1 - \left[1+(t/s)^k\right]^{-(s/\lambda)^k} \xrightarrow[s \to \infty]{} 1 - e^{-(t/\lambda)^k} \tag{14}$$

Similarly, the Hopfenberg model, i.e., Eq. (6), is exactly recovered if $k = 1$, $\lambda = a/n$ and $s = -a$, that is

$$1 - \left[1+(t/s)^k\right]^{-(s/\lambda)^k} \xrightarrow[k=1,\, s=-a,\, \lambda=a/n]{} 1 - (1 - t/a)^n \tag{15}$$

In addition, the first two terms in the Taylor expansion of the generalized Weibull model are equivalent to the Peppas–Sahlin model, i.e., to Eq. (10), namely

$$1 - \left[1+(t/s)^k\right]^{-(s/\lambda)^k} \approx (t/\lambda)^k - \frac{1+(\lambda/s)^k}{2}(t/\lambda)^{2k} \xrightarrow[k=m,\, \lambda = C_1^{-1/m}]{s = \left[-C_1/\left(C_1^2+2C_2\right)\right]^{1/m}} C_1 t^m + C_2 t^{2m} \tag{16}$$

if and only if $C_1^2 + 2C_2 < 0$. These results are summarized in Table 1.

3. Performance of the generalized Weibull dissolution model

The versatility of the proposed dissolution model, i.e., of equation (13), is demonstrated using selected experimental data from published dissolution tests of pharmaceutical

formulations. Specifically, the goodness of fit of the generalized Weibull dissolution model is quantified using the coefficient of determination (R-squared) and the Akaike information criterion (AIC) (Cascone, 2017) when compared against the classical and widely used Weibull dissolution model, i.e.,

$$\mathrm{AIC} = 2\Delta\pi - n\ln\left(\mathrm{SSE}_{\mathrm{Weibull}}/\mathrm{SSE}_{\mathrm{GWeibull}}\right) \tag{17}$$

where n is the number of experimental data points, $\Delta\pi = 1$ is the difference between the number of parameters of the models, and $\mathrm{SSE}_{\mathrm{Weibull}}$ and $\mathrm{SSE}_{\mathrm{GWeibull}}$ are the sum of squared error of the classical Weibull and the generalized Weibull dissolution models, respectively. The lower the AIC value, the better the fitting of the proposed dissolution model compared to the classical Weibull model (Burnham and Anderson, 2004). It is worth noting that even though the Peppas-Sahlin model exhibits a non-monotonic fractional dissolution rate, its performance is not better than the generalized Weibull model and, thus, it is not used in this study.

Eleven cases are summarized in Table 2. It is evident from the table that the generalized Weibull model exhibits a superior behavior (i.e., low AIC values) when the fractional dissolution rate is of non-monotonic type (see cases 8 to 11). However, the generalized Weibull dissolution model returns the classical Weibull model (i.e., $s \to \infty$ and $\mathrm{AIC} \to 2$) when the fractional dissolution rate is of increasing type (see cases 1 to 7). By way of example, Fig. 4 shows the dissolution profiles of cases 9 to 11, that is a blend of 45% microcrystalline cellulose (Avicel PH102; FMC Corporation, Philadelphia), 45% lactose (Pharmatose; DMV International, Veghel, Netherlands), 9% micronized acetaminophen (APAP; Mallinckrodt Inc., Raleigh, NC) and 1% magnesium stearate (MgSt; Mallinkcrodt Inc., St Louis), with different levels of shear strain imparted during the mixing process (Pingali et al., 2011).

In addition, nine cases of atorvastatin tablets are studied and summarized in Table 3, since they exhibit a non-monotonic fractional dissolution rate. These cases correspond to different atorvastatin products, namely innovator, branded, and generic, and to different buffer media, namely solutions with pH1.2, pH4.5 and pH6.8 (Prihapsara, 2020). It is evident from the table that the non-monotonic fractional dissolution rate is captured better by the generalized Weibull dissolution model. By way of example, Fig. 5 shows the fraction of drug release profile of the atorvastatin innovator tablet (Prihapsara, 2020), together with the corresponding fractional dissolution rate profile. Lastly, the performance of the generalized Weibull dissolution model proposed in this work is illustrated in the pie chart in Fig. 6 for all twenty cases.

4. A reduced order model of pharmaceutical tablet dissolution for continuous manufacturing

Dissolution tests are time-consuming destructive tests used as surrogates for in-vivo drug release and bioavailability of drugs, and they are traditionally performed off-line (FDA and CDER, 1997). However, by leveraging data collected both off-line and in real-time (i.e., at-line and in-line), reduced order dissolution models can be used to predict dissolution profiles

in real-time and, thus, facilitate RTRT and QbC strategies. To this end, the relationship between CPPs, CMAs and the dissolution profile of solid tablets must be established (see, e.g., Zaborenko et al. (2019)), namely the effects of (i) API concentration (Pawar et al., 2016b; Wenzel et al., 2017), (ii) crystal size distribution (Chu et al., 2012; Nagy et al., 2021), (iii) lubricant (e.g., concentration (Uzunović and Vranić, 2007) and shear strain Hernandez et al. (2016), Pingali et al. (2011)), (iv) glidant (Pingali et al., 2011) (v) moisture content in powder blend (Steendam et al., 2000, 2001), (vi) compaction force (Pingali et al., 2011; Pawar et al., 2016b), and (vii) tablet porosity (Hattori and Otsuka, 2011). Specifically, Hernandez et al. (2016) studied the effect of shear strain on dissolution and predicted dissolution behavior for different lubrication conditions by using NIRS in combination with multivariate data analysis. Pingali et al. (2011) studied the impact of both glidant (e.g., silica) and lubricant (e.g., magnesium stearate) on dissolution behavior in the context of direct compaction, by means of PCA algorithm and NIR data. Steendam et al. (2000) investigated the effect of moisture content and tablet porosity on dissolution. Chu et al. (2012) observed that the dissolution rate of poorly soluble drugs is strongly related to the particle size distribution of the API. It is worth noting that despite the large body of experimental work to establish the relationship between CPPs, CMAs, and dissolution profiles, mechanistic and semi-mechanistic ROMs of pharmaceutical tablet dissolution for realizing QbC and RTRT frameworks in continuous manufacturing are still scarce or nonexistent.

In the previous section we established that there is a need for a dissolution ROM suitable for a wide range of product formulations, i.e., for robust knowledge management in the context of Industry 4.0, and we proposed the generalized Weibull dissolution model to overcome this limitation. In the next section, immediate release formulations are used to bear out the capabilities of the ROM. Hence, disintegration is an integral step for dissolution of these formulations. Specifically, tablet wicking, also referred to as wetting or liquid uptake due to capillary action, initiates swelling, strain recovery, and dissolution, and, in turn, is considered a prerequisite for tablet disintegration (Markl and Zeitler, 2017; Quodbach and Kleinebudde, 2016). According to Markl and Zeitler (2017), wicking is affected by manufacturing process parameters, processing route, and raw material properties. Therefore, in this section, we will illustrate the extension of this model to capture disturbances in tablet porosity, lubrication conditions, and moisture content in the powder bed—when other CPPs or CMAs are kept constant.

First, the dose of the solid product is written in terms of tablet weight W and API concentration $x_{\mathrm{API}}(\mathrm{w/w})$, that is $M_\infty = W x_{\mathrm{API}}$. Second, Pingali et al. (2011) established that lubrication of pharmaceutical blends using MgSt induces hydrophobicity in the API particles. In turn, this stain-induced hydrophobicity in blends results in tablets with decreasing drug release rate. Here, lubrication entails both a CMA and a CPP, namely the concentration of lubricant added to the formulation and the total shear strain imparted to the blend during the mixing process. In this section, for convenience, we adopt the number of revolutions in a Couette cell as a proxy for total shear strain imparted to the blend (see Pingali et al. (2011)) and, for simplicity, we restrict attention to studies where the lubricant concentration is kept constant. Third, Hattori and Otsuka (2011) observed that for increasing

tablet porosity, the rate of water penetration inside the tablet increases. Steendam et al. (2000) explained that tablets with higher porosity undergo faster disintegration, thus, higher area for the drug to dissolve, and faster dissolution. Fourth, we will show that moisture content effects can be effectively captured by a tableting ROM capable of predicting changes in tablet porosity due to changes in blend moisture fraction. Therefore, the generalized Weibull model (13) is then written as follows

$$M(t; W, x_{\mathrm{API}}, \gamma, \varepsilon) = W x_{\mathrm{API}} \left[1 - \left[1 + [t/s(\gamma,\varepsilon)]^{k(\gamma,\varepsilon)} \right]^{-[s(\gamma,\varepsilon)/\lambda(\gamma,\varepsilon)]^{k(\gamma,\varepsilon)}} \right] \tag{18}$$

where the parameters of the ROM are functions of the total shear imparted to the powder blend, $\gamma \in [0, \infty)$, and the table porosity, $\varepsilon \in [0, \varepsilon_c)$, namely $\lambda(\gamma, \varepsilon)$, $k(\gamma, \varepsilon)$ and $s(\gamma, \varepsilon)$, with the critical porosity ε_c being the smallest porosity at which a tablet is formed. It is worth noting that $\varepsilon = 0$ corresponds to the fully compacted powder, while $\varepsilon = \epsilon_c$ is assumed here to be equivalent to the loose powder blend. On the same token, the total shear strain will always be larger than zero, since the blend components must be blended to attain content uniformity (e.g., γ_0 prior to lubricant mixing). The scenario of a fully lubricated and mixed blend is characterized in the limit by $\gamma \to \infty$. Therefore, these limits are such that at infinite lubrication and zero porosity, drug release is very slow; whereas at zero lubrication or shear strain and critical porosity, drug release is the fastest.

We next propose a systematic procedure to build functions $\lambda(\gamma, \varepsilon)$, $k(\gamma, \varepsilon)$ and $s(\gamma, \varepsilon)$. The procedure is based on the mechanistic limiting behavior described above and summarized in Table 4, where, e.g., $\lambda_0^0 \equiv \lambda(0{,}0)$ and $\lambda_0^{\mathrm{API}} \equiv \lambda(0, \varepsilon_c)$. Specifically, we draw from multivariate rational interpolation and use rational polynomials (Cuyt and Verdonk, 1985) for the model parameters in Eq. (18). In general, a rational function $f(X, Y)$ with second-degree numerator and denominator is given by

$$f(X,Y) = \frac{p_1 X^2 + p_2 Y^2 + p_3 XY + p_4 X + p_5 Y + p_6}{q_1 X^2 + q_2 Y^2 + q_3 XY + q_4 X + q_5 Y + 1} \tag{19}$$

where $X \equiv \gamma \in [0, \infty)$ and $Y \equiv \varepsilon_c/\varepsilon - 1 \in [0, \infty)$. A rational function of a lower degree does not exhibit coupling between γ and ε (i.e., between X and Y). Furthermore, the least number of terms that captures this limiting behavior is such that $p_1 = p_2 = q_1 = q_2 = 0$. Hence, the four limits of interest are $f(0{,}0) = p_6$, $f\left(0, \infty\right) = \lim_{Y \to \infty} \frac{p_5 Y + p_6}{q_5 Y + q_6} = p_5/q_5$, $f\left(\infty, 0\right) = \lim_{X \to \infty} \frac{p_4 X + p_6}{q_4 X + q_6} = p_4/q_4$, and $f(\infty, \infty) = p_3/q_3$. Lastly, the function is bounded within its domain if $q_3 XY + q_4 X + q_5 Y + 1 \neq 0$ which is automatically fulfilled if q_3, q_4 and q_5 are positive numbers. Lastly, since λ, k and s are positive, p_3, p_4, p_5 and p_6 are also positive numbers. .

The rational polynomials of lowest degree that interpolate the mechanistic limiting behavior shown in Table 4 are then given by

$$\begin{aligned}\lambda(\gamma,\varepsilon) &= \frac{\lambda_\infty^0 a_\lambda \gamma(\varepsilon_c/\varepsilon-1)+\lambda_\infty^{\mathrm{API}} b_\lambda \gamma+\lambda_0^0 c_\lambda(\varepsilon_c/\varepsilon-1)+\lambda_0^{\mathrm{API}}}{a_\lambda \gamma(\varepsilon_c/\varepsilon-1)+b_\lambda \gamma+c_\lambda(\varepsilon_c/\varepsilon-1)+1}\\ k(\gamma,\varepsilon) &= \frac{k_\infty^0 a_k \gamma(\varepsilon_c/\varepsilon-1)+k_\infty^{\mathrm{API}} b_k \gamma+k_0^0 c_k(\varepsilon_c/\varepsilon-1)+k_0^{\mathrm{API}}}{a_k \gamma(\varepsilon_c/\varepsilon-1)+b_k \gamma+c_k(\varepsilon_c/\varepsilon-1)+1}\\ s(\gamma,\varepsilon) &= \frac{s_\infty^0 a_s \gamma(\varepsilon_c/\varepsilon-1)+s_\infty^{\mathrm{API}} b_s \gamma+s_0^0 c_s(\varepsilon_c/\varepsilon-1)+s_0^{\mathrm{API}}}{a_s \gamma(\varepsilon_c/\varepsilon-1)+b_s \gamma+c_s(\varepsilon_c/\varepsilon-1)+1}\end{aligned} \tag{20}$$

with all positive model parameters.

Lastly, we have developed a parameter identification method based on a nonlinear multivariate maximization problem. The proposed ROM of pharmaceutical tablet dissolution for continuous manufacturing has 3×7 model parameters, i.e., the functions $\lambda(\gamma,\varepsilon)$, $k(\gamma,\varepsilon)$ and $s(\gamma,\varepsilon)$ has 7 model parameters each. The method is based on the similarity factor f_2 described in the FDA dissolution guidance (FDA and CDER, 1997), i.e., two dissolution profiles are similar if $f_2 = 100$, and are equivalent if $f_2 > 50$. Specifically, the method maximizes the similarity factor f_2 (or minimizes $100 - f_2$) between dissolution experimental data $\mathscr{E}^i$ and model predictions $\mathscr{M}^i$ by choosing optimal model parameters $\overline{\mathscr{P}}$, that is

$$\overline{\mathscr{P}} = \arg\min_{\mathscr{P}\in\mathbb{R}_+^{3\times 7}} \boldsymbol{\Phi}(\mathscr{P}) = \arg\min_{\mathscr{P}\in\mathbb{R}_+^{3\times 7}} \sum_{i=1}^{M} 100 - f_2\left(\mathscr{M}^i(\mathscr{P}) - \mathscr{E}^i\right) \tag{21}$$

with the error measurement functions given by the similarity factor

$$f_2\left(\mathscr{M}^i - \mathscr{E}^i\right) = 50\log\left\{100\left[1+\frac{1}{N_i}\left\|\mathscr{M}^i - \mathscr{E}^i\right\|^2\right]^{-0.5}\right\} \tag{22}$$

where M is the number of dissolution experimental sets, N_i is the number of data points in the ith experimental set, $\|\cdot\|$ is the L2-norm, and the set of model parameters is given by

$$\mathscr{P} \equiv \begin{Bmatrix} \lambda_\infty^0 a_\lambda & \lambda_\infty^{\mathrm{API}} b_\lambda & \lambda_0^0 c_\lambda & \lambda_0^{\mathrm{API}} & a_\lambda & b_\lambda & c_\lambda \\ k_\infty^0 a_k & k_\infty^{\mathrm{API}} b_k & k_0^0 c_k & k_0^{\mathrm{API}} & a_k & b_k & c_k \\ s_\infty^0 a_s & s_\infty^{\mathrm{API}} b_s & s_0^0 c_s & s_0^{\mathrm{API}} & a_s & b_s & c_s \end{Bmatrix} \tag{23}$$

It is worth noting that parameters such as $\lambda_\infty^0 a_\lambda$ must be identified as a lump term so that $\lambda_\infty^0 \to \infty$ can be automatically captured by $a_\lambda \to 0$ and $\lambda_\infty^0 a_\lambda \neq 0$. The nonlinear multivariate minimization problem was solved in MATLAB (MATLAB version 9.8.0.1380330 , R2020a) using the constrained optimization function `fmincon` with the default interior-point algorithm. Furthermore, the proposed model suggests that 7 sets of dissolution experimental data are necessary (but not sufficient) to have a well-posed parameter identification optimization problem (i.e., $M \geq 7$ over a diverse range of processing conditions).

We close by describing the estimation of confidence intervals of model predictions. For convenience, the set of model parameters is recast as a vector $\mathscr{P} \in \mathbb{R}_+^{21}$, and the covariance matrix is approximated as

$$\mathrm{cov}_{\mathscr{P}} \approx \frac{\boldsymbol{\Phi}\left(\overline{\mathscr{P}}\right)}{\mathrm{dof}}\left[\nabla^2\boldsymbol{\Phi}\left(\overline{\mathscr{P}}\right)\right]^{-1} \tag{24}$$

where the objective function $\boldsymbol{\Phi}$, i.e., Eq. (21), and its Hessian $\nabla^2\boldsymbol{\Phi}$ are evaluated at the optimal model parameters $\overline{\mathscr{P}}$ (see, e.g. Casas-Orozco et al. (2021), Barz et al. (2015), Fessler (1996)). In the above equation, the degrees of freedom dof are the difference between the number of data points and the number of model parameters. It is worth noting that all examples of application studied in this work result in a non-diagonal covariance matrix, i.e., model parameters are correlated with respect to each other. Hence, we assume that the model parameters are multivariate Gaussian random variable $\mathscr{N}\left(\overline{\mathscr{P}}, \mathrm{cov}_{\mathscr{P}}\right)$ which, for simplicity, is sampled using a Monte Carlo approach to derive confidence intervals of, for example, model functions $\lambda(\gamma,\varepsilon), k(\gamma,\varepsilon)$ and $s(\gamma,\varepsilon)$, and of model predictions such as the time to release 50% of the API (see, e.g., Tripathy et al. (2016)). In the next two sections, we illustrate this procedure for selected cases.

5. Examples of application

The versatility and the capability of the ROM to represent the dissolution profile of different pharmaceutical formulations and its connection with CPPs and CMAs, namely total shear strain imparted during lubrication γ and table porosity ε, is borne out by the following examples:

1. Effect of lubrication on acetaminophen tablets
2. Combined effect of porosity and moisture content on amylodextrin tablets
3. Effect of porosity on riboflavin tablets
4. Combined effect of lubrication and porosity on acetaminophen tablets
5. Effect of porosity on indomethacin tablets

The proposed dissolution model, i.e., Eqs. (18), is calibrated to experimental dissolution data using the nonlinear multivariate minimization problem, i.e., Eqs. (21) and (22), to estimate the optimal set of model parameters (23).

5.1. Effect of lubrication on acetaminophen tablets

This case study is retrieved from the work of Pingali et al. (2011). The formulation consisted of 45% microcrystalline cellulose (Avicel PH102; FMC Corporation, Philadelphia), 45% lactose (Pharmatose; DMV International, Veghel, Netherlands), 9% acetaminophen (APAP; Mallinckrodt Inc., Raleigh, NC) and 1% magnesium stearate (MgSt; Mallinkcrodt Inc., St Louis), all % w/w. The powders were mixed in a 3.8-liter V blender for 10 min to obtain a homogeneous mixture of lubricant and excipients. Next, controlled shear was applied in a Couette shear cell at a shear rate of 80rpm. The powders were exposed to a minimum, average, and maximum strain by applying shear strains of 40rev, 160rev, and 640rev. Target tablet weight was 500mg. Compression force of 8kN was applied to obtain the compacted

tablets. Hence, tablet porosity was kept constant at $\bar{\varepsilon}$ and shear strain was varied with $\gamma = \gamma_0 + \{40,160,640\}$ rev. Therefore, Eq. (20) is simplified as follows

$$\begin{aligned} \lambda(\gamma,\bar{\varepsilon}) &= \frac{\lambda_\infty^0 a_\lambda \gamma(\varepsilon_c/\bar{\varepsilon}-1)+\lambda_\infty^{\mathrm{API}} b_\lambda \gamma+\lambda_0^0 c_\lambda(\varepsilon_c/\bar{\varepsilon}-1)+\lambda_0^{\mathrm{API}}}{a_\lambda \gamma(\varepsilon_c/\bar{\varepsilon}-1)+b_\lambda \gamma+c_\lambda(\varepsilon_c/\bar{\varepsilon}-1)+1} \\ \Rightarrow \lambda(\gamma) &= \frac{\lambda_\infty^{\bar{\varepsilon}} d_\lambda \gamma+\lambda_0^{\bar{\varepsilon}}}{d_\lambda \gamma+1} \\ k(\gamma) &= \frac{k_\infty^{\bar{\varepsilon}} d_k \gamma+k_0^{\bar{\varepsilon}}}{d_k \gamma+1} \\ s(\gamma) &= \frac{s_\infty^{\bar{\varepsilon}} d_s \gamma+s_0^{\bar{\varepsilon}}}{d_s \gamma+1} \end{aligned} \tag{25}$$

where d_λ, d_k and d_s are model parameters, and $\{\lambda_\infty^{\bar{\varepsilon}}, k_\infty^{\bar{\varepsilon}}, s_\infty^{\bar{\varepsilon}}\}$ and $\{\lambda_0^{\bar{\varepsilon}}, k_0^{\bar{\varepsilon}}, s_0^{\bar{\varepsilon}}\}$ correspond to the limiting behavior at full lubrication and no lubrication conditions, respectively. Lastly, Pingali et al. (2011) performed dissolution tests in 900 mL of phosphate buffer solution with a pH of 5.8 at temperature $37.0 \pm 0.5^{\circ}$C for 90 min. The tests were done on a USP II apparatus at 50rpm. The API absorbance was measured at 243 nm, and sampling was performed every 2 minutes.

Model parameters are successfully estimated and reported in Fig. 7(a). It is evident from Fig. 7(c) that as the total shear imparted to the blend increases, the dissolution process is delayed and, thus, the time to release 50% of the API increases, and plateaus at high values of strain. Interestingly, the fractional dissolution rate transitions from a decreasing trend, at low levels of shear, to a non-monotonic trend, at higher levels of shear (see the vertical line in Fig. 7(c)). This observation reinforces the need for a dissolution model capable of capturing all fractional dissolution rates observed experimentally. Fig. 8 provides insight into the reasons for this transition, since λ and k increase with shear strain, while s decreases, with $k = 1$ at ~180 rev. The goodness of the estimation is exemplified by the similarity factor between each set of predicted and measured dissolution profiles, i.e., $f_2 > 50$ (FDA and CDER, 1997) (see Fig. 7(b)), the narrow confidence interval of model predictions (see Fig. 7(c)) and model parameters (see Fig. 8). Interestingly, a wider confidence interval at high shear strain indicates that additional experimental evidence is needed to lower the uncertainty in the predictions.

5.2. Combined effect of porosity and moisture content on amylodextrin tablets

This case study is retrieved from the work of Steendam et al. (2000). This formulation consisted of 10% theophylline monohydrate (OPG Farma, Utrecht, The Netherlands) and 90% amylodextrin powders (AVEBE, Foxhol, The Netherlands), both %w/w. The mixture was mixed in a Turbula mixer at 90rpm for 30 min to obtain different moisture fractions. After adding lubricant, (0.5%) magnesium stearate, additional blending was performed for 2 min. Cylindrically flat-faced amylodextrin compacts were obtained of weight 500mg and a diameter of 13 mm. Different compaction pressures were applied to prepare the compacts on a hydraulic press. The load rate was 2kN/s and the hold time was 0.1 s. Porosities of the tablets were calculated from the weight and dimensions of the tablets and the true densities of the powders. Different moisture fractions of the powder blend led to different

final porosity of the tablets. Since shear strain was kept constant at $\bar{\gamma}$, Eq. (20) is simplified as follows

$$\begin{aligned}\lambda(\bar{\gamma},\varepsilon) &= \frac{\lambda_{\infty}^{0}a_{\lambda}\bar{\gamma}(\varepsilon_c/\varepsilon-1)+\lambda_{\infty}^{\mathrm{API}}b_{\lambda}\bar{\gamma}+\lambda_{0}^{0}c_{\lambda}(\varepsilon_c/\varepsilon-1)+\lambda_{0}^{\mathrm{API}}}{a_{\lambda}\bar{\gamma}(\varepsilon_c/\varepsilon-1)+b_{\lambda}\bar{\gamma}+c_{\lambda}(\varepsilon_c/\varepsilon-1)+1}\\ \Rightarrow \lambda(\varepsilon) &= \frac{\lambda_{\bar{\gamma}}^{0}e_{\lambda}(\varepsilon_c/\varepsilon-1)+\lambda_{\bar{\gamma}}^{\mathrm{API}}}{e_{\lambda}(\varepsilon_c/\varepsilon-1)+1}\\ k(\varepsilon) &= \frac{k_{\bar{\gamma}}^{0}e_{k}(\varepsilon_c/\varepsilon-1)+k_{\bar{\gamma}}^{\mathrm{API}}}{e_{k}(\varepsilon_c/\varepsilon-1)+1}\\ s(\varepsilon) &= \frac{s_{\bar{\gamma}}^{0}e_{s}(\varepsilon_c/\varepsilon-1)+s_{\bar{\gamma}}^{\mathrm{API}}}{e_{s}(\varepsilon_c/\varepsilon-1)+1}\end{aligned} \tag{26}$$

where e_{λ}, e_{k} and e_{s} are model parameters, and $\{\lambda_{\bar{\gamma}}^{0}, k_{\bar{\gamma}}^{0}, s_{\bar{\gamma}}^{0}\}$ and $\{\lambda_{\bar{\gamma}}^{\mathrm{API}}, k_{\bar{\gamma}}^{\mathrm{API}}, s_{\bar{\gamma}}^{\mathrm{API}}\}$ correspond to the limiting behavior for fully compacted powder and loose powder blend, respectively. Lastly, Steendam et al. (2000) performed dissolution tests in 900 mL of phosphate buffer solution with a pH of 6.8 at temperature 37.0 ± 0.5°C. The tests were done on a USP II apparatus at 100rpm. The API absorbance was measured at 268 nm.

Model parameters are successfully estimated and reported in Fig. 9(a). The goodness of the estimation is exemplified by the similarity factor between each set of predicted and measured dissolution profiles, i.e., $f_2 > 50$ (FDA and CDER, 1997) (see Fig. 9(b)). It is evident from Fig. 9(c) that as tablet porosity increases, the dissolution process becomes faster and, thus, the time to release 50% of the API decreases. Interestingly, the fractional dissolution rate transitions from a non-monotonic trend, at low tablet porosity, to a decreasing trend, at high tablet porosity (see the vertical line in Fig. 9(c)). This observation reinforces the need for a dissolution model capable of capturing all fractional dissolution rates observed experimentally. Fig. 10 provides insight into the reasons for this transition, since λ and k decrease with porosity, while s increases, with $k = 1$ at ~0.18 porosity value.

It is well-known that moisture content has an effect on dissolution profile and, thus, it is another CMA to be considered in the context of process design, optimization, and control. Steendam et al. (2001) extended the experimental study described above to investigate the effect of moisture fraction on amylodextrin tablets. They observed that tablets fabricated using the same compaction pressure, but under different moisture conditions, have different dissolution profiles. It is argued that moisture has plasticizing and lubricating effects in amylodextrin and, thus, it facilitates deformation of the excipient particles, i.e., of the glassy polymer. This is evident in Fig. 11(a) for porosities above 0.09, i.e., as the moisture content increases, less compaction pressure is needed to attain a given tablet porosity. The trend is non-monotonic and more complex at porosities below 0.09. Alternatively, the figure indicates that tablets fabricated using the same compaction pressure, but under different moisture conditions, have different porosities—which, in turn, is a result of different in-die table porosity and different elastic recovery after table ejection from the die. We demonstrate next that once the tablet microstructure is formed, dissolution only depends on the tablet porosity, not the moisture content of the powder. The generalization of this statement to other formulations and pharmaceutical products is beyond the scope of this work.

Steendam et al. (2001) performed dissolution tests of tablets fabricated using different compaction pressure, with a load rate of 2kN/s and hold time of 0.1 s, and five different moisture fractions. Fig. 11(b) shows the t_{50} value of these tests as a function of the measured tablet porosity. The existence of a unique relationship is evident from the figure. The figure additional shows the t_{50} value predicted by the model calibrated to the experimental dissolution profiles shown in Fig. 9, that is to the dissolution of tablets fabricated at a single moisture fraction. The agreement between experimental observations and model predictions is remarkable. Specifically, the model predicts the following time to release 50% of the API

$$t_{50} = s\left[2^{(\lambda/s)^k} - 1\right]^{1/k} \tag{27}$$

where $\lambda(\varepsilon), k(\varepsilon)$ and $s(\varepsilon)$ are given by Eq. (26). Evidently, to realize the vision conveyed in Fig. 1, i.e., to realize QbC and RTRT frameworks in continuous manufacturing, a compaction ROM that captures the complex relationship between tablet porosity, compaction pressure σ, and moisture fraction MF is needed, i.e., the function $\varepsilon(\sigma, \text{MF})$ is needed.

5.3. Effect of porosity on riboflavin tablets

This case study is retrieved from the work of Hattori and Otsuka (2011). This formulation consisted of 0.5% riboflavin (Wako pure chemicals, Tokyo), 1% magnesium stearate (NOF Corporation, Tokyo), and 98.5% α-lactose monohydrate (Pharmatose 200M; DMV-Fonterra Exipients, Nörten-Haddenberg, Germany), all %w/w. The powder blend was mixed for 5 min. Cylindrically flat-faced compacts were obtained of weight 100mg and a diameter of 8 mm Tablet porosity was controlled by compaction pressure, and all other process parameters were fixed. Therefore, Eq. (26) was used to estimate the model parameters and limiting behavior of this formulation. Lastly, Hattori and Otsuka (2011) performed dissolution tests in distilled water at temperature 37.0 ± 0.5 °C for 90 min. The tests were done on a USP II apparatus at 50rpm. The API absorbance was measured at 266 nm.

Model parameters are successfully estimated and reported in Fig. 12(a). The goodness of the estimation is exemplified by the similarity factor between each set of predicted and measured dissolution profiles, i.e., $f_2 > 50$ (FDA and CDER, 1997) (see Fig. 12(b)). It is evident from Fig. 12(c) that as tablet porosity increases, the dissolution process becomes faster and, thus, the time to release 50% of the API decreases and it is equal to the t_{50} of pure API at critical porosity. Interestingly, the fractional dissolution rate transitions from a non-monotonic trend, at low tablet porosity, to a decreasing trend, at high tablet porosity (see the vertical line in Fig. 12(c)). This observation reinforces the need for a dissolution model capable of capturing all fractional dissolution rates observed experimentally. Fig. 13 provides insight into the reasons for this transition, since λ and k decrease with porosity, while s increases, with $k = 1$ at ~ 0.16 porosity value.

5.4. Combined effect of lubrication and porosity on acetaminophen tablets

This case study is retrieved from the work of Callegari et al. (2013). The formulation for this case study consisted of 90% lactose, 9% acetaminophen, and 1% magnesium stearate,

all %w/w. To obtain a homogeneous preblend of lubricant and excipients, all the powders were pre-mixed in a V-blender. A total of seven tablets were prepared and grouped into two different sets, namely tablets with different porosity values and no controlled shear applied (i.e., compression force of 8 to 40kN, or pressure of 102 to 510MPa, with 18 to 6% porosity), and tablets with different controlled shear applied and same compaction force (i.e., controlled shear of 0, 160 and 640rev, with 8kN compaction force or 15% porosity). Therefore, Eq. (20) was used to estimate the model parameters and limiting behavior of this formulation. Lastly, Callegari et al. (2013) performed dissolution tests in 900 mL of pH5.8 phosphate buffer at temperature 37.0 ± 0.5°C. The tests were done on a USP II apparatus at 50rpm. The API absorbance was measured at 243 nm, and sampling was performed every 3 min with a total of 90-150 min allocated for the dissolution test.

We close this example by illustrating that the semi-mechanistic nature of the dissolution ROM proposed in this work allows for identifying model parameters from experimental observations that are not strictly dissolution tests of solid tablets. Firstly, the limiting behavior of the model at critical porosity is assumed to correspond to the dissolution behavior of loose API crystals. Specifically, the set of parameters $\{\lambda_0^{\text{API}}, k_0^{\text{API}}, s_0^{\text{API}}\}$ can be identified from a dissolution test of API crystals. Alternatively, if only the t_{50}^{API} is available, the following expression can be used as an equality constrain to the nonlinear multivariate minimization problem (21),

$$t_{50}^{\text{API}} = s_0^{\text{API}} \left[2^{\left(\lambda_0^{\text{API}}/s_0^{\text{API}}\right) k_0^{\text{API}}} - 1 \right]^{1/k_0^{\text{API}}} \tag{28}$$

The t_{50} value of pure acetaminophen crystal was obtained from the dissolution test performed by Albertini et al. (2004) in 900 mL of pH 6.8 phosphate buffer at temperature 37.0 ± 0.1 °C. Though the buffer media of pure API dissolution is different from tablet dissolution, that value was still used as an equality constraint to the nonlinear optimization problem to highlight different capabilities of the model. Secondly, the critical porosity ε_c is readily available from tablet hardness tests, or tensile strength curves, by means of the Leuenberger equation (see, e.g., Razavi et al. (2018)), that is from

$$\sigma_t(\epsilon) = \sigma_0 \left[1 - \frac{\varepsilon e^{\varepsilon_c - \varepsilon}}{\varepsilon_c} \right] \tag{29}$$

where σ_0 is the tensile strength of a fully dense tablet, that is of a tablet with zero porosity. Pawar et al. (2016a) have reported tensile strength measurements for the formulation used in this example at different values of total shear imparted to the blend (see Fig. 15). These experimental data reveal that the sensitivity of critical porosity to changes in lubrication is small and that the estimated values are between 0.1520 and 0.1714, with an average of $\varepsilon_c = 0.1645$. Naturally, in the context of QbC and RTRT frameworks, tableting and dissolution (semi-)mechanistic ROMs would be related to each other by sharing the same critical porosity. Hence, ε_c was assumed known in the model parameter estimation.

Model parameters are successfully estimated and reported in Fig. 14(a). The goodness of the estimation is exemplified by the similarity factor between each set of predicted and measured dissolution profiles, i.e., $f_2 > 50$ (FDA and CDER, 1997) (see Fig. 14(b)). It is evident from Fig. 14(c) that as tablet porosity increases and shear imparted to the blend decreases, the dissolution process becomes faster and, thus, the time to release 50% of the API decreases. Interestingly, the fractional dissolution rate transitions from an increasing trend, at low tablet porosity, to a non-monotonic trend, at high tablet porosity, and, lastly, to a decreasing trend at critical porosity (see the dotted curves in Fig. 14(c)). This figure not only depicts the design space for this formulation (i.e., for QbD) but it also serves as a tool to identify optimal control conditions (i.e., for QbC) where the target product profile (TPP) is the least sensitive to changes in operating conditions or, more precisely, to the CPPs most difficult tightly control. It bears emphasis that these observations reinforce the need for a dissolution model capable of capturing all fractional dissolution rates observed experimentally.

5.5. Effect of porosity on indomethacin tablets

This case study is retrieved from the work of Bawuah et al. (2021). The formulation for this case study consisted of 39.1% microcrystalline cellulose (Avicel PH-102; FMC Europe NV, Brussels, Belgium), 46.9% lactose anhydrous (Supertab21AN; DFE pharma, Goch, Germany), 3% croscarmellose sodium (DuPont Nutrition, Wilmington DE, USA), 10% indomethacin (Sigma-Aldrich Company Ltd., Gillingham, UK), and 1% magnesium stearate (Fisher Scientific, Fair Lawn NJ, USA), all % w/w. All the powders except magnesium stearate were mixed for 10 mins and then magnesium stearate was added and mixed for 1 more min at 32 rpm. Biconvex tablets were made of five different porosity levels using a compaction simulator. The thickness of the tablets was varied to obtain different porosity values and all the tablets had a target weight of 400mg. All other process conditions were fixed. Therefore, Eq. (26) was used to estimate the model parameters. Lastly, the dissolution tests of the indomethacin tablets were performed in 900 mL of pH 6.2 phosphate buffer media at temperature 37.0 ± 0.5 °C. The tests were done on a USP II apparatus at 50rpm. The API absorbance was measured at 265 nm. Sampling was performed every 80 s.

Model parameters are successfully estimated and reported in Fig. 16(a). The goodness of the estimation is exemplified by the similarity factor between each set of predicted and measured dissolution profiles, i.e., $f_2 > 50$ (FDA and CDER, 1997) (see Fig. 16(b)). It is worth noting that the experimental data in Fig. 16(c) shows a non-monotonic trend with porosity that occurred due to the swelling of the disintegrant (croscarmellose sodium) at higher tablet porosity. According to Bawuah et al. (2021), water penetration or wicking rate inside a tablet is faster with increasing porosity, thus faster swelling, disintegration, and dissolution. However, at higher tablet porosity, this phenomenon is not always true if the disintegrant forms a gel layer which prolongs disintegration and dissolution time. The formation of gel constricts the pore space and thus slows down the wicking rate. Similar type of non-monotonic t_{50} trend due to tablet swelling is also observed by Callegari et al. (2013) for a formulation that consisted of 45% microcrystalline cellulose, 45% lactose, 9% acetaminophen, and 1% magnesium stearate (all % w/w). Callegari et al. (2013) reported

that the volumetric swelling rate $\left(\mathrm{mm}^3/\mathrm{s}\right)$ of tablets also shows a non-monotonic trend with changing tablet porosity and the faster a tablet swells, the faster it releases the drug. Our proposed ROMs capture this non-monotonic trend in t_{50}, as shown in Fig. 16(c). Interestingly, the fractional dissolution rate is non-monotonic for any tablet porosity. Fig. 17 provides insight into the reasons for this kind of fractional dissolution rate, since λ decreases and k increases with porosity, while s decreases, with $k > 1$ at any porosity value.

6. Parameter estimation of the ROMs for lomustine tablets

Lomustine (trade name Gleostine, a capsule) is a widely used oral antineoplastic agent for the treatment of primary and metastatic brain tumors (Kaina et al., 2007). As tablets are stable, cost-effective, easy to manufacture, handle and swallow, and have a longer shelf life, we illustrate the model parameter estimation of the ROM presented in Section 4 for lomustine solid tablets to, in turn, assist product design and manufacturing (albeit the latter are beyond the scope of this work). In contrast to the examples presented in Section 5, and to the best of our knowledge, dissolution testing conditions for lomustine products are not available in the open literature. Therefore, we specifically illustrate: (i) the identification of a plausible formulation, (ii) the development of a dissolution protocol to characterize lomustine tablets, (iii) the fabrication of lomustine tablets with different porosity and using different lubrication conditions, in the context of a direct compaction manufacturing route (see Fig. 1), and (iv) the estimation of model parameters from a representative set of dissolution profiles.

Commercial lomustine capsules, i.e., Gleostine capsules, are reported to contain mannitol, MgSt, lactose, and the gelatin capsule shell as excipients (Biotechnology, 2017; Lomustine “medac” 40 mg - Summary of Product Characteristics (SmPC) - (emc), 2020). In this work, by way of illustration, we adopt a blend with 4.41% lomustine, 70.59% lactose monohydrate (Pharmatose; DFE pharma), 24% mannitol (D-mannitol; Sigma-Aldrich), and 1% MgSt (Acros Organics), all % w/w. Hence, a 114mg lomustine tablet will correspond to a 5mg dose of lomustine (cf. Gleostine capsules with 10mg, 40mg, and 100mg doses). Lomustine crystals used in this study were provided by Mackey et al. (2020) manufactured by a small-scale hybrid manufacturing system.

Lomustine is a water-insoluble API; hence, a dissolution protocol for lomustine tablets was developed following Noory et al. (2002). Firstly, the effect of buffer medium pH on the lomustine product was evaluated. Solubility of solid tablets in media of pH 1.2, 4.5, and 6.8 was characterized by collecting samples at 10, 20, 30, 60, 90, and 120 min. A buffer medium of pH 6.8 (i.e., a 0.05 M phosphate buffer) was chosen because the excipients did not show any interference at the wavelength of lomustine’s peak absorbance. Secondly, the smallest amount of surfactant in the buffer medium was determined. Sodium lauryl sulfate (SLS) is the most widely used surfactant to increase the solubility of a water-insoluble API, and it was added in 1% w/w to the medium of pH6.8 to achieve greater than 85% dissolution in 90 min. Following the U.S. Pharmacopeia (USP, 2011) guidelines (cf., the European Pharmacopoeia and the Japanese Pharmacopoeia for similar guidelines), the dissolution specifications adopted are listed in Table 5. Furthermore, a Distek 2100C dissolution system

was used to perform all dissolution tests, and a UV-1600PC UV/Vis Spectrophotometer was used to perform the quantitative analysis of the dissolution samples at 231 nm – lomustine shows a peak absorbance at 231 nm, and the excipients do not.

Following the examples of application discussed in Section 5 and in the context of a direct compaction manufacturing route, the effect of tablet porosity and lubrication conditions were investigated. Firstly, the following three experiments were carried out and reported in Fig. 18 to investigate the effect of lubrication:

1. Using the 250 – 355 μm sieve size range, 15mg of lomustine crystal were lubricated with 1%w/w MgSt and mixed for 3 minutes in a 16ml glass vial, and three dissolution tests were performed, using 5mg each. From the same sieve size range but with no lubrication, three more dissolution tests were performed, using 5mg each. Fig. 18(b) shows that the dissolution profiles are similar within error.
2. Using the 0 – 180 μm sieve size range, two lomustine formulations were prepared using 4.41% lomustine, 69.59% (and 71.34%) lactose monohydrate, 24% mannitol, and 2% (and 0.25%) MgSt, all %w/w. Both blends were mixed for 5 min in a 16ml glass vial. Three 114mg, 6 mm, flat-faced tablets of each formulation were fabricated in a Gamlen D Series bench-top compaction simulator to an in-die porosity of 0.15 or relative density of 0.85. Fig. 18(c) shows that the dissolution profiles are similar within error.
3. Using the 0 – 180μm sieve size range, two lomustine formulations were prepared using 4.41% lomustine, 69.59% (and 71.59%) lactose monohydrate, 24% mannitol, and 2% (and 0%) MgSt, all %w/w. Both blends were mixed for 5 min in a 16ml glass vial. Three 114mg, 6 mm, flat-faced tablets of each formulation were fabricated in a Gamlen D Series bench-top compaction simulator to an in-die porosity of 0.05 or relative density of 0.95. Fig. 18(d) shows that the dissolution profiles are similar within error.

It is evident from the figures that lomustine crystals and tablets exhibit negligible sensitivity to MgSt lubrication conditions (i.e., $\lambda_0^{\mathrm{API}} = \lambda_\infty^{\mathrm{API}} = \lambda_{\bar{z}}^{\mathrm{API}}$, etc.). Secondly, the characterization of tablets with three different relative densities was carried out and reported in Fig. 19 to investigate the effect of tablet porosity. Specifically, using the 125-250 μm sieve size range, a lomustine formulation was prepared using 4.41% lomustine, 70.59% lactose monohydrate, 24% mannitol, and 1%MgSt, all %w/w. A total of 1200mg of the unlubricated blend was mixed for 1 min in a 20ml glass vial to obtain a homogeneous blend. Next, MgSt was added to the blend and mixed for an additional 3 min. Flat-faced, 114mg, 6 mm tablets were fabricated in a Gamlen D Series bench-top compaction simulator to 0.05, 0.10, and 0.15 in-die porosity. Six tablets were fabricated under each category, three of which were used to measure dissolution profile, potency, and, thus, content uniformity, while the another three were used to measure tablet dimensions and hardness after 17 h. Tensile strength was calculated and reported in Fig. 19(a), and the critical tablet porosity, i.e., the smallest porosity at which a tablet is formed, was estimated using (29) to be $\varepsilon_c = 0.23$. Elastic recovery was calculated and reported in Fig. 19(b), and it was parameterized by

$$\varepsilon = \varepsilon_{\mathrm{id}} + \epsilon_0(1 - \varepsilon_{\mathrm{id}}/\varepsilon_{\mathrm{c},\epsilon})(1 - \varepsilon_{\mathrm{id}}) \tag{30}$$

where, $\varepsilon_{\mathrm{id}}$ is the in-die porosity of the tablet (i.e., porosity at peak compaction pressure inside the die), $\varepsilon_{\mathrm{c},\epsilon}$ is a critical porosity, which is typically larger or equal to the jamming porosity of the blend (here $\varepsilon_{\mathrm{c},\epsilon} = 0.33$), and ϵ_0 is the elastic recovery at zero in-die porosity (here $\epsilon_0 = 0.12$) (Gonzalez, 2019). Compaction force is reported in Fig. 19(c) and the loading path was parameterized by the Kawakita compaction model, that is by

$$F = \frac{\pi D^2}{4b}\left[a\frac{1 - \varepsilon_{\mathrm{id}}}{\varepsilon_{\mathrm{c},F} - \varepsilon_{\mathrm{id}}} - 1\right]^{-1} \tag{31}$$

where D is the tablet diameter, a and b are model parameters, and $\varepsilon_{\mathrm{c},F}$ is a critical porosity typically similar to the jamming porosity of the blend (here $a = 0.52, b = 0.11\mathrm{MPa}^{-1}$ and $\varepsilon_{\mathrm{c},F} = 0.51$). It is worth noting that $\varepsilon_{\mathrm{c},F} > \varepsilon_{\mathrm{c},\epsilon} > \varepsilon_{\mathrm{c}} > \varepsilon$.

Lastly, three lomustine tablets of each condition (i.e., of porosity 0.05, 0.10 and 0.15) were characterized following the dissolution protocol established above and summarized in Table 5. Since lomustine crystal exhibits negligible sensitivity to lubrication, the dissolution profile of loose API crystals was also used to in the model parameter estimation of Eq. (26)—see Fig. 20(a). The critical porosity ε_{c} is readily available from tensile strength curves (Fig. 19(a)). It is evident from Fig. 20(c) that as tablet porosity increases, the dissolution process becomes faster and, thus, the time to release 50% of the API decreases. Interestingly, the fractional dissolution rate transitions from a non-monotonic trend, at low tablet porosity, to an increasing trend, at high tablet porosity (see the vertical line in Fig. 20(c)). This observation reinforces the need for a dissolution model capable of capturing all fractional dissolution rates observed experimentally. Fig. 21 provides insight into the reasons for this transition, since λ and k decrease with porosity with $k > 1$ at any porosity value, while s increases, the time at which maximum fractional dissolution rate occurs also increases. Thus the fractional dissolution rate becomes increasing at higher porosity.

The goodness of the estimation is exemplified by the similarity factor between each set of predicted and measured dissolution profiles, i.e., $f_2 > 50$ (FDA and CDER, 1997) (see Fig. 20(b)), the narrow confidence interval of model predictions (see Fig. 20(c)) and model parameters (see Fig. 21). Interestingly, a wider confidence interval at low tablet porosity indicates that additional experimental evidence is needed to lower the uncertainty in the predictions. In complex experimental campaigns where multiple CPPs and CMAs are varied, this uncertainty quantification can be used to build a *sequential design of experiment approach* that maximizes the expected information gain and minimizes the number of experiments, if beyond the scope of this paper (see, e.g., Pandita et al. (2019) and references therein).

6.1. An outlook of RTRT in continuous manufacturing

We close this study by demonstrating the applicability of the proposed semi-mechanistic reduced order model of pharmaceutical tablet dissolution to QbC and RTRT in continuous manufacturing. Specifically, and in the context of tableting, weight variability is assumed

to follow a normal distribution (Fig. 22(a)) with a mean value equal to $\bar{W} = 114\text{mg}$ and a relative standard deviation equal to $\sigma_W/\bar{W} = 1\%$, i.e., $W \equiv \mathcal{N}(\bar{W}, \sigma_W^2)$. The mean model parameter $\bar{\mathcal{P}}$ reported in Fig. 20(a), of the otherwise multivariate Gaussian random variable $\mathcal{N}(\bar{\mathcal{P}}, \text{cov}_{\mathcal{P}})$, is used for clarity of illustration. Perfect content uniformity is assumed for the same lomustine formulation characterized above, i.e., for $x_{\text{API}} = 4.41\%$ lomustine ($125 - 250\mu\text{m}$ sieve size range), 70.59% lactose monohydrate, 24% mannitol, and 1% MgSt. Two idealized states of control strategies to attain a target product porosity of $\varepsilon = 0.146$ (i.e., an in-die porosity of $\varepsilon_{\text{id}} = 0.05$) are studied, namely (i) the punch separation at peak force is kept constant, and (ii) the compaction force is kept constant. Next, the impact of weight variability on CQAs of lomustine tablets is investigated using the formulae established in this work.

For the state of control where the punch separation at peak force is kept constant and equal to $H_{\text{id}} = 2.78$ mm, the relative frequency distribution of in-die porosity (Fig. 22(b)) is determined from the weight variability (Fig. 22(a)) as follows

$$\varepsilon_{\text{id}} = 1 - 4W/\pi D^2 H_{\text{id}} \rho_{\text{t}}$$

where ρ_{t} is the true density of the blend. The relative frequency distribution of compaction force (Fig. 22(c)) follows from Eq. (31), and the relative frequency distribution of tablet potency (Fig. 22(d)), porosity (Fig. 22(e)) and tensile strength (Fig. 22(f)) from Wx_{API}, Eq. (30), and Eq. (29), respectively. The relative frequency distribution of tablet height (Fig. 22(g)) is estimated by assuming that the diameter of the tablet does not change significantly upon ejection and, thus,

$$H = 4W/\pi D^2 \rho_{\text{t}}(1 - \varepsilon)$$

Lastly, the relative frequency distribution of time to release half of the target product dosage (Fig. 22(h)) and the relative frequency distribution of the similarity factor with respect to the target product profile (Fig. 22(i)) are determined to aid RTRT.

For the state of control where the compaction force is kept constant and equal to $F = 3.48\text{kN}$, the in-die porosity is in turn also kept constant and equal to $\varepsilon_{\text{id}} = 0.05$, and the relative frequency distribution of punch separation at peak force (Fig. 23(b)) is determined from weight variability as follows

$$H_{\text{id}} = 4W/\pi D^2 \rho_{\text{t}}(1 - \varepsilon_{\text{id}})$$

While tablet potency and tablet height follow the relative frequency distributions shown in Figs. 23(c) and 23(d), the tablet porosity and tensile strength are kept constant and equal to $\varepsilon = 0.146$ and $\sigma_{\text{t}} = 0.64\text{MPa}$. Despite all tablets having the target product porosity, both the time to release half of the target product dosage and the similarity factor with respect to the target product profile vary, and the corresponding relative frequency distributions are shown in Figs. 23(e) and 23(f).

RTRT in continuous manufacturing aims to reduce production cost and time by eliminating the need for extensive end-product quality testing, but not without embracing the need for sophisticated PATs and ROMs (Markl et al., 2020). For example, uncertainty in the measurements due to CPPs disturbance or CMAs variance is inevitable and, hence, model-based data reconciliation emerges as an effective real-time process management tool to accomplish robust process monitoring and control. Specifically, redundancy in the PAT sensor network and data correlation based on process understanding (e.g., on mechanistic and semi-mechanistic ROMs) can be exploited to (i) design a process control structure effective in reducing product quality variability (Su et al., 2018, 2019b), (ii) facilitate data reconciliation in real-time (see, e.g., Moreno et al. (2019), Su et al. (2019a)), and, eventually, (iii) mitigate control degradation due to plant-model mismatch (Huang et al., 2021). Figs. 22 and 23 illustrate that, for the same weight variability conditions, different control strategies naturally result in different product quality variability (cf. Fig. 22(f) and $\sigma_t = 0.64$MPa, or Figs. 22(i) and 23(f)). It is worth noting that some of the CPPs and CQAs presented in these figures, such as tablet weight (Su et al., 2019a), punch separation, in-die porosity, compaction force, tablet potency (De Leersnyder et al., 2018; Ward et al., 2013), tablet dimensions (Moes et al., 2008), and tablet porosity (Bawuah et al., 2020, 2021; Donoso et al., 2003; Hakulinen et al., 2008), can be directly or indirectly measured in real-time to estimate relative frequency distributions; whereas other CQAs, such as tablet tensile strength and dissolution, require destructive at-line or off-line testing (see Fig. 1). The latter, however, can be estimated by proxy of a non-destructive test, such as an ultrasound measurement of Young's modulus which correlates with tensile strength for known CMAs Razavi et al. (2016). Similarly, it has been shown that the dissolution profile can be estimated from near-infrared spectroscopy data for known CMAs Pawar et al. (2016b). Ultimately, one can envision that these advanced PATs will be integrated with a (semi-)mechanistic dissolution ROM, such as the formulae presented in this work, a (semi-)mechanistic tableting ROM that estimates weight variability and incorporates lubricant, glidant, and API concentration effects (Bachawala et al., 2022; Bommireddy and Gonzalez, 2022), to realize RTRT from a plan-wide model-based data reconciliation module.

7. Future directions

We close by pointing out some limitations of our approach and possible avenues for extending this line of work. First, we have restricted attention to direct compaction and investigated the effect of tablet porosity and the total amount of shear strain imparted to the blend during lubrication. The systematic extension of the model to other CPPs and CMAs of relevance, such as the lubricant concentration, is a worthwhile direction for future research. Second, the crystal size distribution of poorly water-soluble drugs is strongly related to dissolution rate (Chu et al., 2012; Hintz and Johnson, 1989; Anderberg, 1994). The semi-mechanistic nature of the presented approach can only capture these effects by recourse of extensive training with experimental data using, e.g, machine learning algorithms (Galata et al., 2021). A mechanistic dissolution model of API crystals and its integration with a (semi-)mechanistic model of tablet wetting, swelling, and disintegration are desirable, if beyond the scope of this paper. Third, the integration of this approach with in-line and at-line PAT available in continuous manufacturing lines and the realization of QbC and

RTRT frameworks remain the ultimate goal of this line of work and a promising research direction.

8. Conclusion

We have proposed a generalization of the Weibull dissolution model, referred to as *generalized Weibull dissolution model*, that seamlessly captures all three fractional dissolution rates experimentally observed in pharmaceutical solid tablets, namely decreasing, increasing, and non-monotonic rates. This is in contrast to traditional reduced order models, which capture at most two fractional dissolution rates and, thus, are not suitable for a wide range of product formulations hindering, for example, the adoption of knowledge management in the context of Industry 4.0. Using the Akaike information criterion, we have shown that the proposed model greatly outperforms the traditional Weibull dissolution model when the formulation exhibits a non-monotonic fractional dissolution rate. Furthermore, we have extended the generalized Weibull dissolution model to capture the relationship between CPPs, CMAs, and dissolution profiles to, in turn, facilitate RTRT and QbC strategies. Specifically, we have endowed the model with multivariate rational polynomials that interpolate the mechanistic limiting behavior of tablet dissolution as CPPs and CMAs approach certain values of physical significance (such as the upper and lower bounds of tablet porosity or lubrication conditions), thus the semi-mechanistic nature of the ROM. Lastly, we have developed a parameter identification method based on a nonlinear multivariate maximization problem of the f_2 similarity factor between dissolution experimental data and model predictions. Restricting attention to direct compaction and using various case studies from the literature, we have demonstrated the versatility and the capability of the semi-mechanistic ROM to estimate changes in dissolution due to process disturbances in tablet porosity, lubrication conditions (i.e., the total amount of shear strain imparted during blending), and moisture content in the powder blend. Finally, we have formulated and fabricated lomustine solid tablets, characterized their tableting and dissolution behavior, and estimated model parameters for a tableting-dissolution ROM to illustrate the applicability of the proposed work to QbC and RTRT in continuous manufacturing. In all of the cases considered in this work, the estimations of the proposed semi-mechanistic reduced order model of pharmaceutical dissolution are in remarkable agreement with experimental data.

Acknowledgments

This research is supported by the U.S. Food and Drug Administration through Grant No. 1U01FD006738-01, 5U01FD006738-02, and 5U01FD006738-03 entitled “Risk-based process synthesis and Industry 4.0 framework for pharmaceutical manufacturing processes”. The authors gratefully acknowledge Gamlen Instruments (London, UK) for the availability of the Gamlen D Series bench-top compaction simulator, and Professor Tonglei Li at Purdue University for providing access to the Distek 2100C dissolution system. The authors would also like to express gratitude to Dr. Jaron Mackey and Professor Zoltan Nagy at Purdue University for manufacturing the lomustine crystals used in the experiments reported in this paper.

Data availability

Data will be made available on request.

References

Albertini B, Cavallari C, Passerini N, Voinovich D, Gonzalez-Rodriguez ML, Magarotto L, Rodriguez L, 2004. Characterization and taste-masking evaluation of acetaminophen granules: comparison between different preparation methods in a high-shear mixer. Eur. J. Pharm. Sci 21 (2–3), 295–303. [PubMed: 14757501]

Anderberg EK, 1994. Studies on the dissolution of fine particulate practically insoluble drugs and on the effect of surface active enhancers on gastrointestinal absorption of hydrophilic drugs.

Bachawala S, Nasilowski D, Gonzalez M, 2022. Semi-mechanistic reduced order model of pharmaceutical tablet compaction for continuous manufacturing: Lubricant and glidant effects. (in preparation), Unpublished Results.

Barz T, Körkel S, Wozny G, et al. , 2015. Nonlinear ill-posed problem analysis in model-based parameter estimation and experimental design. Comput. Chem. Eng 77, 24–42.

Bawuah P, Markl D, Farrell D, Evans M, Portieri A, Anderson A, Goodwin D, Lucas R, Zeitler JA, 2020. Terahertz-based porosity measurement of pharmaceutical tablets: a tutorial. J. Infrared Millim. Terahertz Waves 41 (4), 450–469.

Bawuah P, Markl D, Turner A, Evans M, Portieri A, Farrell D, Lucas R, Anderson A, Goodwin DJ, Zeitler JA, 2021. A fast and non-destructive terahertz dissolution assay for immediate release tablets. J. Pharm. Sci 110 (5), 2083–2092. [PubMed: 33307044]

Biotechnology, N., 2017. Material safety data sheet of gleostine.

Bommireddy Y, Gonzalez M, 2022. Semi-mechanistic reduced order model of pharmaceutical tablet compaction for continuous manufacturing: Active ingredient concentration effects. (in preparation) Unpublished Results.

Bruschi ML, 2015. Mathematical Models of Drug Release. Vol. 63, Woodhead Publishing Cambridge, UK.

Burnham KP, Anderson DR, 2004. Multimodel inference: understanding AIC and BIC in model selection. Sociol. Methods Res 33 (2), 261–304.

Byrn S, Futran M, Thomas H, Jayjock E, Maron N, Meyer RF, Myerson AS, Thien MP, Trout BL, 2015. Achieving continuous manufacturing for final dosage formation: challenges and how to meet them. May 20–21, 2014 continuous manufacturing symposium. J. Pharm. Sci 104 (3), 792–802.

Callegari G, Awad T, Wang Y, Pawar P, Pastrana I, Drazer G, Muzzio FJ, Cuitino A, 2013. The effect of blend shearing and compression on dissolution dynamics for immediate release tablets. In: AIChE Annual Meeting.

Casas-Orozco D, Laky D, Wang V, Abdi M, Feng X, Wood E, Laird C, Reklaitis GV, Nagy ZK, 2021. PharmaPy: An object-oriented tool for the development of hybrid pharmaceutical flowsheets. Comput. Chem. Eng 153, 107408.

Cascone S, 2017. Modeling and comparison of release profiles: Effect of the dissolution method. Eur. J. Pharm. Sci 106, 352–361. [PubMed: 28627469]

Chatterjee S, 2012. FDA perspective on continuous manufacturing. In: IFPAC Annual Meeting. Baltimore, MD, Vol. 26, pp. 34–42.

Chu KR, Lee E, Jeong SH, Park E-S, 2012. Effect of particle size on the dissolution behaviors of poorly water-soluble drugs. Arch. Pharm. Res 35 (7), 1187–1195. [PubMed: 22864741]

Costa P, Lobo JMS, 2001. Modeling and comparison of dissolution profiles. Eur. J. Pharm. Sci 13 (2), 123–133. [PubMed: 11297896]

Cuyt AA, Verdonk BM, 1985. Multivariate rational interpolation. Computing 34 (1), 41–61.

De Almeida LP, Simões S, Brito P, Portugal A, Figueiredo M, 1997. Modeling dissolution of sparingly soluble multisized powders. J. Pharm. Sci 86 (6), 726–732. [PubMed: 9188056]

De Leersnyder F, Peeters E, Djalabi H, Vanhoorne V, Van Snick B, Hong K, Hammond S, Liu AY, Ziemons E, Vervaet C, et al. , 2018. Development and validation of an in-line NIR spectroscopic method for continuous blend potency determination in the feed frame of a tablet press. J. Pharm. Biomed. Anal 151, 274–283. [PubMed: 29413975]

Ding B, 2018. Pharma Industry 4.0: Literature review and research opportunities in sustainable pharmaceutical supply chains. Process Saf. Environ. Prot 119, 115–130.

Dokoumetzidis A, Papadopoulou V, Macheras P, 2006. Analysis of dissolution data using modified versions of Noyes–Whitney equation and the Weibull function. Pharm. Res 23 (2), 256–261. [PubMed: 16421665]

Donoso M, Kildsig D, Ghaly ES, 2003. Prediction of tablet hardness and porosity using near-infrared diffuse reflectance spectroscopy as a nondestructive method. Pharm. Dev. Technol 8 (4), 357–366. [PubMed: 14601960]

FDA, 2004. Guidance for industry: PAT-A framework for innovative pharmaceutical development, manufacturing and quality assurance. http://www.fda.gov/cder/guidance/published.hml.

FDA, 2012. Guidance for industry: Q11 development and manufacture of drug substances. US department of health and human services.

FDA, CDER, 1997. Guidance for industry: Dissolution testing of immediate release solid oral dosage forms.

FDA, CDER, 2006. Guidance for industry: Q8 pharmaceutical development.

Fessler J, 1996. Mean and variance of implicitly defined biased estimators (such as penalized maximum likelihood): applications to tomography. IEEE Trans. Image Process 5 (3), 493–506. 10.1109/83.491322. [PubMed: 18285134]

Fisher AC, Liu W, Schick A, Ramanadham M, Chatterjee S, Brykman R, Lee SL, Kozlowski S, Boam AB, Tsinontides SC, et al. , 2022. An audit of pharmaceutical continuous manufacturing regulatory submissions and outcomes in the US. Int. J. Pharm 622, 121778. [PubMed: 35500688]

Galata DL, Könyves Z, Nagy B, Novák M, Mészáros LA, Szabó E, Farkas A, Marosi G, Nagy ZK, 2021. Real-time release testing of dissolution based on surrogate models developed by machine learning algorithms using NIR spectra, compression force and particle size distribution as input data. Int. J. Pharm 597, 120338. [PubMed: 33545285]

Gao Y, Vanarase A, Muzzio F, Ierapetritou M, 2011. Characterizing continuous powder mixing using residence time distribution. Chem. Eng. Sci 66 (3), 417–425.

Gonzalez M, 2019. Generalized loading-unloading contact laws for elasto-plastic spheres with bonding strength. J. Mech. Phys. Solids 122, 633–656.

Hakulinen M, Pajander J, Leskinen J, Ketolainen J, Van Veen B, Niinimäki K, Pirskanen K, Poso A, Lappalainen R, 2008. Ultrasound transmission technique as a potential tool for physical evaluation of monolithic matrix tablets. AAPS PharmSciTech 9 (1), 267–273. [PubMed: 18446491]

Hattori Y, Otsuka M, 2011. NIR spectroscopic study of the dissolution process in pharmaceutical tablets. Vib. Spectrosc 57 (2), 275–281.

Hernandez E, Pawar P, Keyvan G, Wang Y, Velez N, Callegari G, Romanach RJ, 2016. Prediction of dissolution profiles by non-destructive near infrared spectroscopy in tablets subjected to different levels of strain. J. Pharm. Biomed. Anal 117, 568–576. [PubMed: 26604167]

Hintz RJ, Johnson KC, 1989. The effect of particle size distribution on dissolution rate and oral absorption. Int. J. Pharm 51 (1), 9–17.

Huang Y-S, Sheriff MZ, Bachawala S, Gonzalez M, Nagy ZK, Reklaitis GV, 2021. Evaluation of a combined MHE-NMPC approach to handle plant-model mismatch in a rotary tablet press. Processes 9 (9).

Kaina B, Christmann M, Naumann S, Roos WP, 2007. MGMT: key node in the battle against genotoxicity, carcinogenicity and apoptosis induced by alkylating agents. DNA Repair 6 (8), 1079–1099. [PubMed: 17485253]

Korsmeyer RW, Gurny R, Doelker E, Buri P, Peppas NA, 1983. Mechanisms of solute release from porous hydrophilic polymers. Int. J. Pharm 15 (1), 25–35.

Kvarnström B, Bergquist B, 2012. Improving traceability in continuous processes using flow simulations. Prod. Plan. Control 23 (5), 396–404.

Lakerveld R, Benyahia B, Braatz RD, Barton PI, 2013. Model-based design of a plant-wide control strategy for a continuous pharmaceutical plant. AIChE J. 59 (10), 3671–3685.

Lánsky P, Weiss M, 1999. Does the dose-solubility ratio affect the mean dissolution time of drugs? Pharm. Res 16 (9), 1470–1476. [PubMed: 10496667]

Lánsky P, Weiss M, 2001. Modeling heterogeneity of particles and random effects in drug dissolution. Pharm. Res 18 (7), 1061–1067. [PubMed: 11496946]

Lánsky P, Weiss M, 2003. Classification of dissolution profiles in terms of fractional dissolution rate and a novel measure of heterogeneity. J. Pharm. Sci 92 (8), 1632–1647. [PubMed: 12884250]

Lawrence XY, Amidon G, Khan MA, Hoag SW, Polli J, Raju G, Woodcock J, 2014. Understanding pharmaceutical quality by design. AAPS J. 16 (4), 771–783. [PubMed: 24854893]

Leane M, Pitt K, Reynolds GK, Dawson N, Ziegler I, Szepes A, Crean AM, Dall Agnol R, Group MCSMW, et al. , 2018. Manufacturing classification system in the real world: factors influencing manufacturing process choices for filed commercial oral solid dosage formulations, case studies from industry and considerations for continuous processing. Pharm. Dev. Technol 23 (10), 964–977. [PubMed: 30320539]

Lee SL, O'Connor TF, Yang X, Cruz CN, Chatterjee S, Madurawe RD, Moore CM, Lawrence XY, Woodcock J, 2015. Modernizing pharmaceutical manufacturing: from batch to continuous production. J. Pharm. Innov 10 (3), 191–199.

Lomustine "medac" 40 mg - Summary of Product Characteristics (SmPC) - (emc), 2020. https://www.medicines.org.uk/emc/product/1401/smpc. (Accessed on 12 May 2021).

Macheras P, Dokoumetzidis A, 2000. On the heterogeneity of drug dissolution and release. Pharm. Res 17 (2), 108–112. [PubMed: 10751023]

Mackey J, Mufti A, Lee S-L, Abdi M, Feng X, Wood E, Thompson DH, Nagy Z, 2020. Process design and development of a small scale hybrid manufacturing system for the cancer drug lomustine. In: 2020 Virtual AIChE Annual Meeting. AIChE.

Markl D, Warman M, Dumarey M, Bergman E-L, Folestad S, Shi Z, Manley LF, Goodwin DJ, Zeitler JA, 2020. Review of real-time release testing of pharmaceutical tablets: State-of-the art, challenges and future perspective. Int. J. Pharm 582, 119353. [PubMed: 32325242]

Markl D, Zeitler JA, 2017. A review of disintegration mechanisms and measurement techniques. Pharm. Res 34 (5), 890–917. [PubMed: 28251425]

MATLAB version 9.8.0.1380330 (R2020a) [Computer software manual], 2020. The Mathworks, Inc., Natick, Massachusetts.

Moes JJ, Ruijken MM, Gout E, Frijlink HW, Ugwoke MI, 2008. Application of process analytical technology in tablet process development using NIR spectroscopy: Blend uniformity, content uniformity and coating thickness measurements. Int. J. Pharm 357 (1–2), 108–118. [PubMed: 18394831]

Moreno M, Ganesh S, Shah YD, Su Q, Gonzalez M, Nagy ZK, Reklaitis GV, 2019. Sensor network robustness using model-based data reconciliation for continuous tablet manufacturing. J. Pharm. Sci 108 (8), 2599–2612. [PubMed: 30904476]

Nagy B, Szilágyi B, Domokos A, Vészi B, Tacsi K, Rapi Z, Pataki H, Marosi G, Nagy ZK, Nagy ZK, 2021. Dynamic flowsheet model development and digital design of continuous pharmaceutical manufacturing with dissolution modeling of the final product. Chem. Eng. J 419, 129947.

Noory C, Tran N, Ouderkirk L, Shah V, 2002. Steps for development of a dissolution test for sparingly water-soluble drug products. Am. Pharm. Rev 5, 16–21.

Noyes AA, Whitney WR, 1897. The rate of solution of solid substances in their own solutions. J. Am. Chem. Soc 19 (12), 930–934.

Pandita P, Bilionis I, Panchal J, 2019. Bayesian optimal design of experiments for inferring the statistical expectation of expensive black-box functions. J. Mech. Des 141 (10).

Pawar P, Joo H, Callegari G, Drazer G, Cuitino AM, Muzzio FJ, 2016a. The effect of mechanical strain on properties of lubricated tablets compacted at different pressures. Powder Technol. 301, 657–664.

Pawar P, Wang Y, Keyvan G, Callegari G, Cuitino A, Muzzio F, 2016b. Enabling real time release testing by NIR prediction of dissolution of tablets made by continuous direct compression (CDC). Int. J. Pharm 512 (1), 96–107. [PubMed: 27543350]

Peppas NA, Sahlin JJ, 1989. A simple equation for the description of solute release. III. Coupling of diffusion and relaxation. Int. J. Pharm 57 (2), 169–172.

Pingali K, Mendez R, Lewis D, Michniak-Kohn B, Cuitiño A, Muzzio F, 2011. Evaluation of strain-induced hydrophobicity of pharmaceutical blends and its effect on drug release rate under multiple compression conditions. Drug Dev. Ind. Pharm 37 (4), 428–435. [PubMed: 20942612]

Prihapsara F, 2020. Evaluation of compared dissolution profile of Atorvastatin tablets in markets. J. Adv. Pharm. Educ. Res 10 (1).

Quodbach J, Kleinebudde P, 2016. A critical review on tablet disintegration. Pharm. Dev. Technol 21 (6), 763–774. [PubMed: 25975586]

Razavi SM, Callegari G, Drazer G, Cuitino AM, 2016. Toward predicting tensile strength of pharmaceutical tablets by ultrasound measurement in continuous manufacturing. Int. J. Pharm 507 (1), 83–89. [PubMed: 27157310]

Razavi SM, Gonzalez M, Cuitiño AM, 2018. Quantification of lubrication and particle size distribution effects on tensile strength and stiffness of tablets. Powder Technol. 336, 360–374

Steendam R, Eissens AC, Frijlink HW, Lerk CF, 2000. Plasticisation of amylodextrin by moisture: Consequences for drug release from tablets. Int. J. Pharm 204 (1–2), 23–33 [PubMed: 11011982]

Steendam R, Frijlink HW, Lerk CF, 2001. Plasticisation of amylodextrin by moisture. Consequences for compaction behaviour and tablet properties. Eur. J. Pharm. Sci 14 (3), 245–254. [PubMed: 11576830]

Su Q, Bommireddy Y, Gonzalez M, Reklaitis GV, Nagy ZK, 2018. Variation and risk analysis in tablet press control for continuous manufacturing of solid dosage via direct compaction. In: Eden MR, Ierapetritou MG, Towler GP (Eds.), 13th International Symposium on Process Systems Engineering. PSE 2018, In: Computer Aided Chemical Engineering, vol. 44, Elsevier, pp. 679–684.

Su Q, Bommireddy Y, Shah Y, Ganesh S, Moreno M, Liu J, Gonzalez M, Yazdanpanah N, O'Connor T, Reklaitis GV, Nagy ZK, 2019a. Data reconciliation in the Quality-by-Design (QbD) implementation of pharmaceutical continuous tablet manufacturing. Int. J. Pharm 563, 259–272. [PubMed: 30951859]

Su Q, Ganesh S, Moreno M, Bommireddy Y, Gonzalez M, Reklaitis GV, Nagy ZK, 2019b. A perspective on Quality-by-Control (QbC) in pharmaceutical continuous manufacturing. Comput. Chem. Eng 125, 216–231. [PubMed: 36845965]

Tripathy R, Bilionis I, Gonzalez M, 2016. Gaussian processes with built-in dimensionality reduction: Applications to high-dimensional uncertainty propagation. J. Comput. Phys 321, 191–223.

USP, 2011. 711 Dissolution.

Uzunović A, Vranić E, 2007. Effect of magnesium stearate concentration on dissolution properties of ranitidine hydrochloride coated tablets. Bosnian J. Basic Med. Sci 7 (3), 279.

Wang J, Flanagan DR, 1999. General solution for diffusion-controlled dissolution of spherical particles. 1. Theory. J. Pharm. Sci 88 (7), 731–738. [PubMed: 10393573]

Ward HW, Blackwood DO, Polizzi M, Clarke H, 2013. Monitoring blend potency in a tablet press feed frame using near infrared spectroscopy. J. Pharm. Biomed. Anal 80, 18–23. [PubMed: 23511228]

Weiss M, 1996. A novel extravascular input function for the assessment of drug absorption in bioavailability studies. Pharm. Res 13 (10), 1547–1553. [PubMed: 8899849]

Wenzel T, Stillhart C, Kleinebudde P, Szepes A, 2017. Influence of drug load on dissolution behavior of tablets containing a poorly water-soluble drug: estimation of the percolation threshold. Drug Dev. Ind. Pharm 43 (8), 1265–1275. [PubMed: 28398095]

Wu H, Lyon RC, Khan MA, Voytilla RJ, Drennen JK III, 2015. Integration of near-infrared spectroscopy and mechanistic modeling for predicting film-coating and dissolution of modified release tablets. Ind. Eng. Chem. Res 54 (22), 6012–6023.

Yu LX, 2008. Pharmaceutical quality by design: product and process development, understanding, and control. Pharm. Res 25 (4), 781–791. [PubMed: 18185986]

Zaborenko N, Shi Z, Corredor CC, Smith-Goettler BM, Zhang L, Hermans A, Neu CM, Alam MA, Cohen MJ, Lu X, et al. , 2019. First-principles and empirical approaches to predicting in vitro dissolution for pharmaceutical formulation and process development and for product release testing. AAPS J. 21 (3), 1–20.

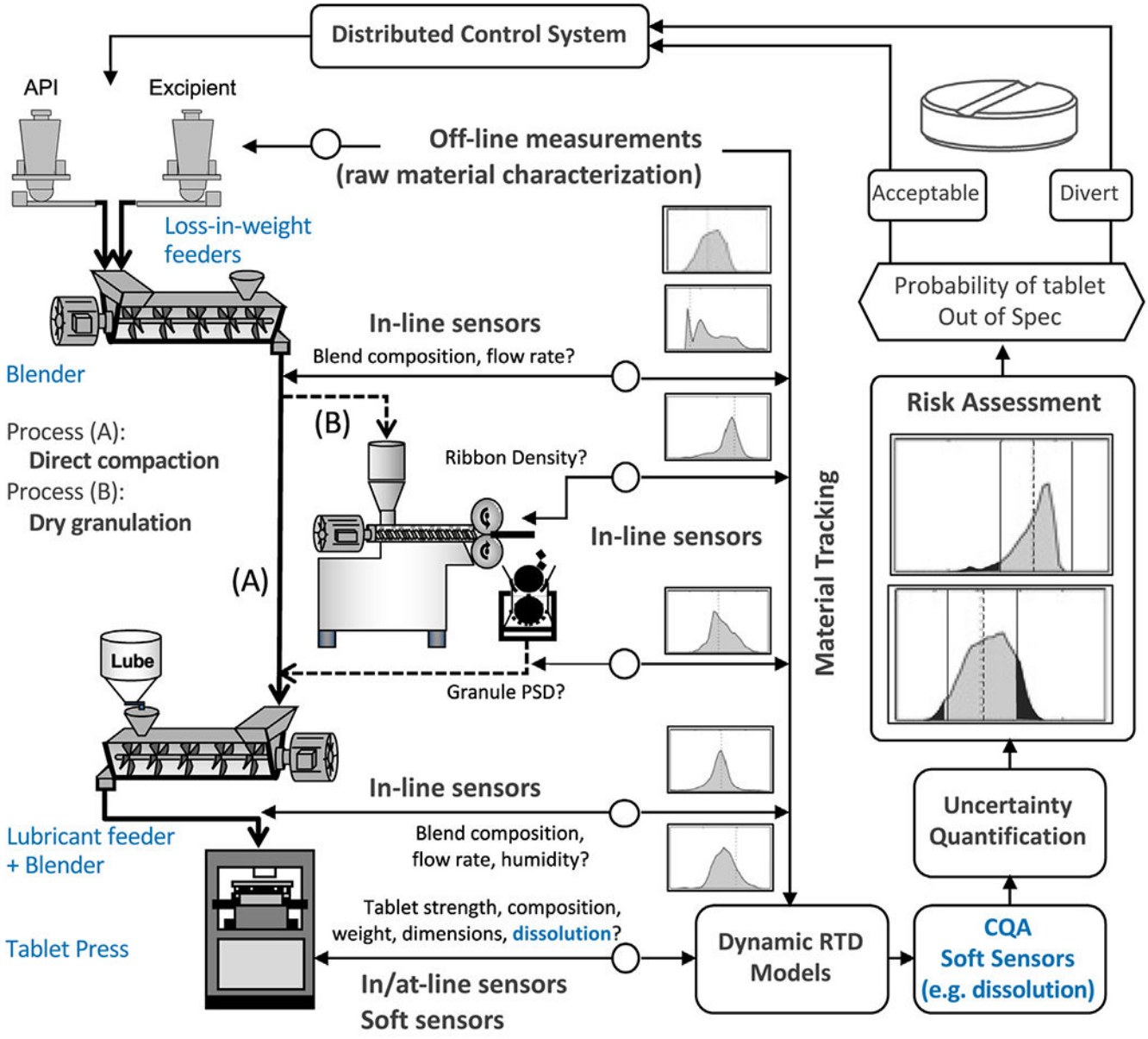

Fig. 1.

Continuous solids processing pilot plant at Purdue University: (i) the API and excipients are fed through K-Tron and Schenck feeders, respectively, and uniformly blended in a Gericke GCM-250 blender, (ii) depending on the manufacturing process, namely direct compaction or dry granulation, the powder blend is next sent to a K-Tron MT12 micro-screw lubricant feeder or an Alexanderwerk WP120 roller compactor for dry granulation, and (iii) solid tablets are produced by a Natoli NP-400 rotary tablet press.

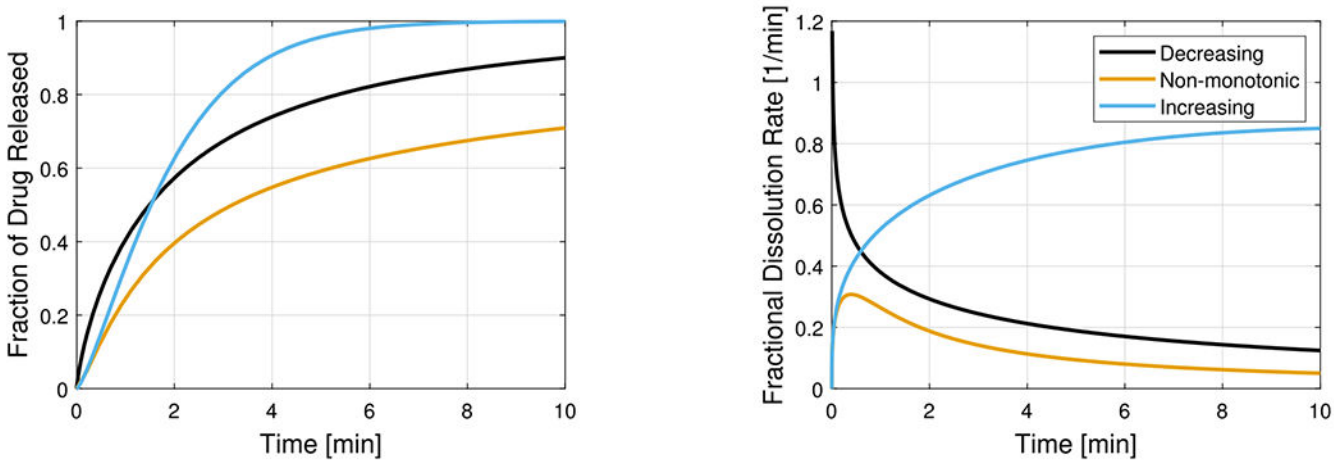

Fig. 2.

Typical shapes of cumulative dissolution profiles, $M(t)/M_{\infty}$ (left) and their corresponding fractional dissolution rate profile, $K(t)$ (right).

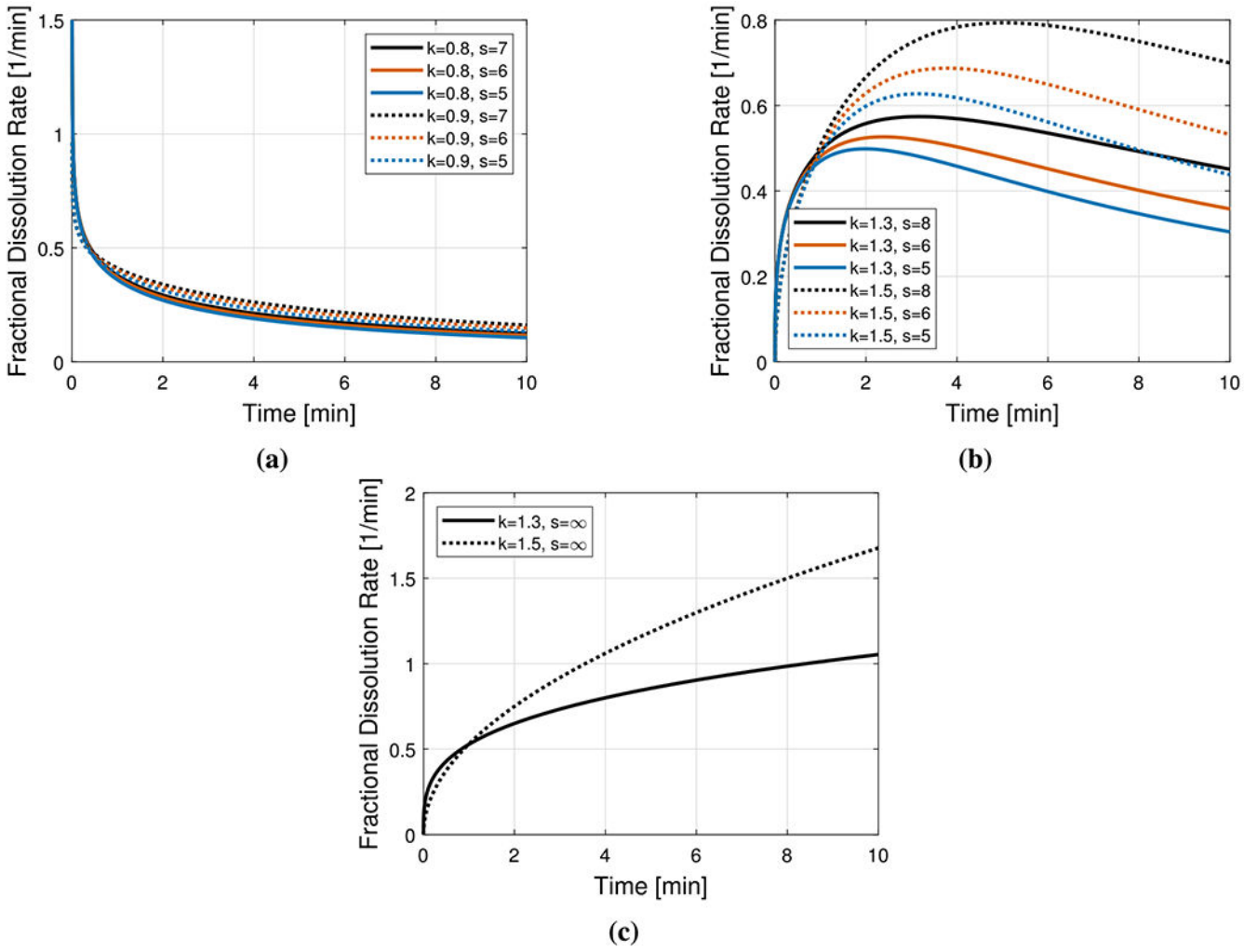

Fig. 3.

The three types of fractional dissolution rates of the generalized Weibull dissolution model. (a) Decreasing fractional dissolution rate type, for $0 < k \leq 1$ and any value of s. (b) Non-monotonic fractional dissolution rate type, for $k > 1$ and any finite value of s. (c) Increasing fractional dissolution rate type, for $k > 1$ and $s \to \infty$.

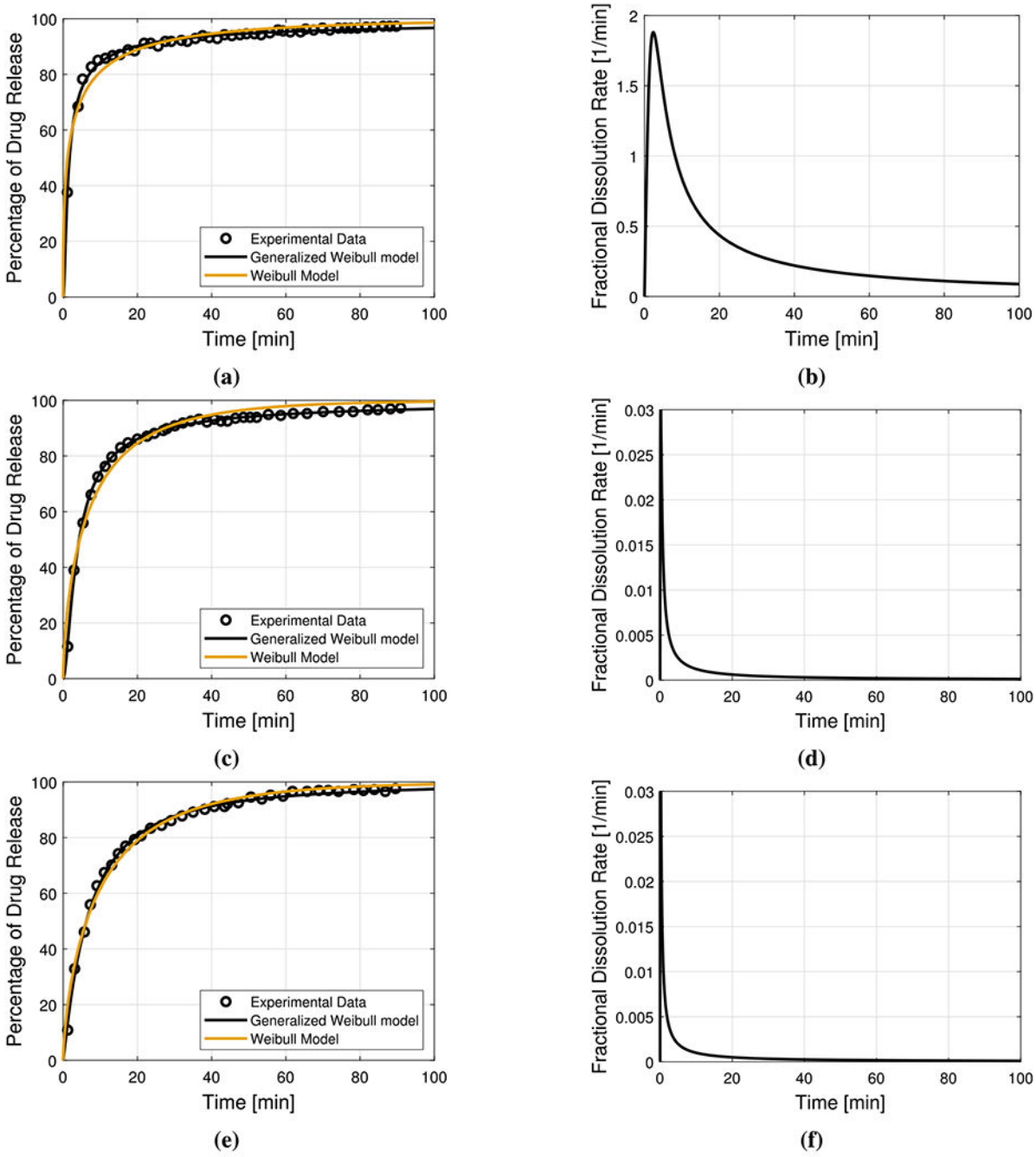

Fig. 4.

Performance of the generalized Weibull dissolution model in reproducing dissolution profiles that exhibit non-monotonic fractional dissolution rates (see Table 2 for R-squared and AIC values). Formulations consist of 9% acetaminophen (APAP), 45% lactose (Pharmatose), 45% microcrystalline cellulose (Avicel PH 102), 1% magnesium stearate (MgSt), all % w/w, mixed in a Couette shear cell at a rate of 80rpm for (a) 40rev, (c) 160rev, and (e) 640 rev (Pingali et al., 2011). The corresponding non-monotonic fractional dissolution rates are shown in (b), (d), and (f), respectively.

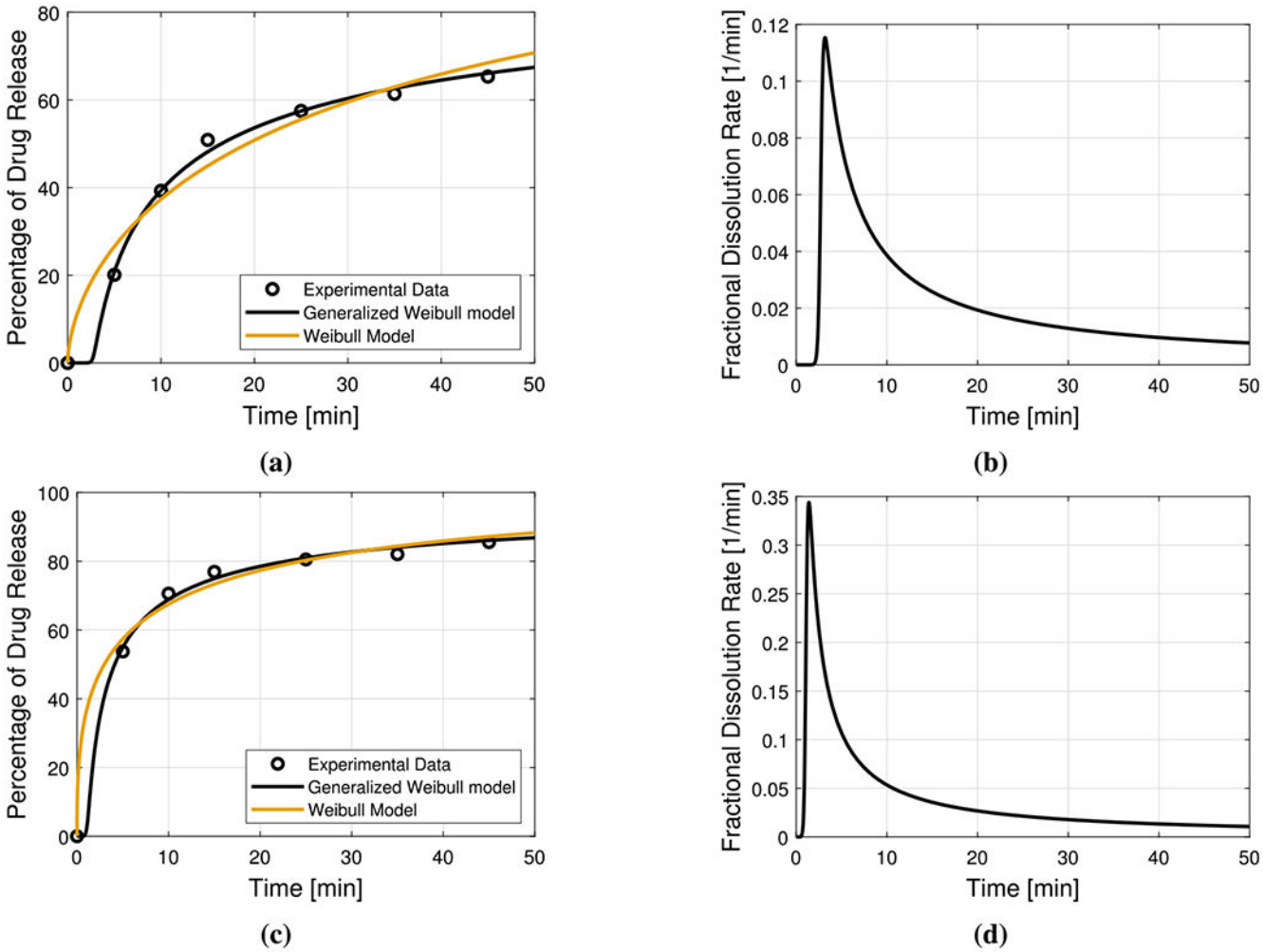

Fig. 5.

Performance of the generalized Weibull dissolution model in reproducing dissolution profiles that exhibit non-monotonic fractional dissolution rates (see Table 3 for R-squared and AIC values). Formulations consist of Atorvastatin Innovator tablets characterized in a buffer media of (a) pH 1.2 and (c) pH 6.8 (Prihapsara, 2020). The corresponding non-monotonic fractional dissolution rates are shown in (b) and (d), respectively.

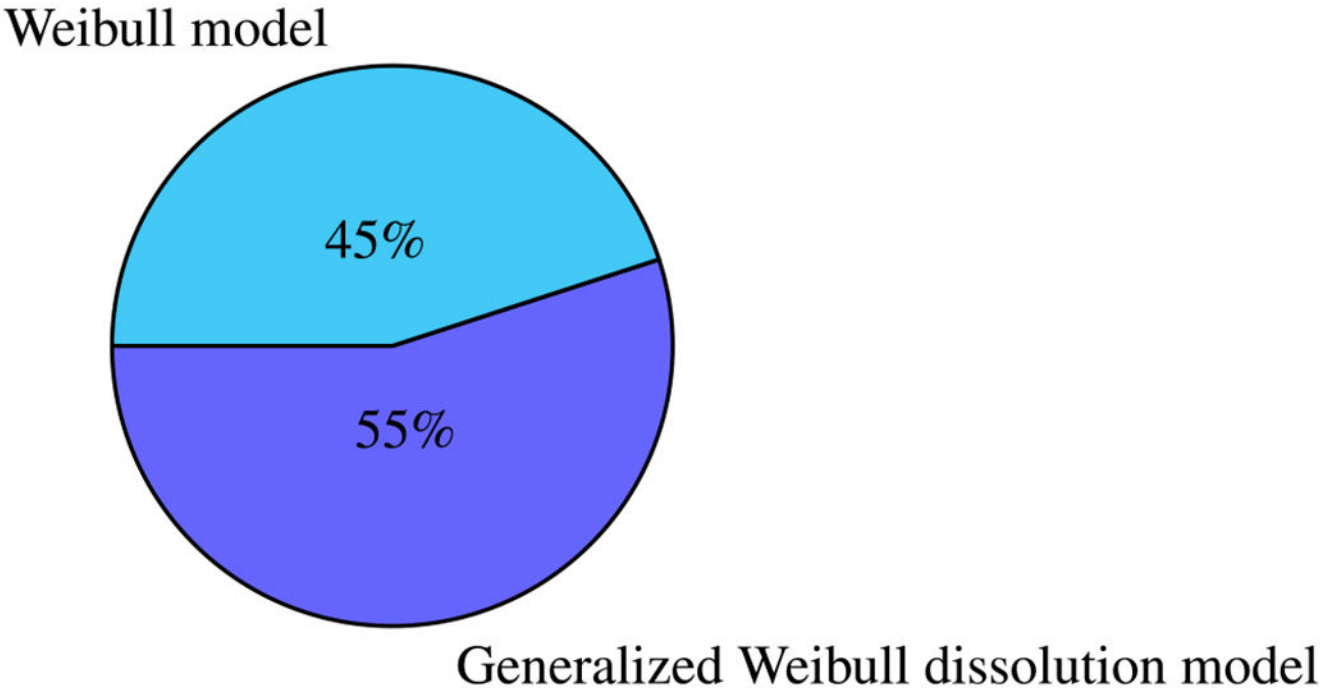

Fig. 6.

Summary of Tables 2 and 3. Out of 20 dissolution profiles, fitting the generalized model is better for 11 dissolution profiles. For the other nine profiles, the generalized model and Weibull model gives the same fitting, but as the Weibull model has only two parameters, it is a better model for these 9 cases.

		Tablet $\varepsilon = \bar{\varepsilon}$
No lubrication	$\gamma = 0$	$\lambda_0^{\bar{\varepsilon}} = 5.28 \times 10^{-7}$ min $k_0^{\bar{\varepsilon}} = 0.37$ $s_0^{\bar{\varepsilon}} = 3.76 \times 10^{7}$ min
Full lubrication	$\gamma \to \infty$	$\lambda_\infty^{\bar{\varepsilon}} = 7.07$ min $k_\infty^{\bar{\varepsilon}} = 1.47$ $s_\infty^{\bar{\varepsilon}} = 5.73$ min

λ	$d_\lambda = 0.01$ rev^{-1}
k	$d_k = 0.01$ rev^{-1}
s	$d_s = 5.67 \times 10^{5}$ rev^{-1}

(a)

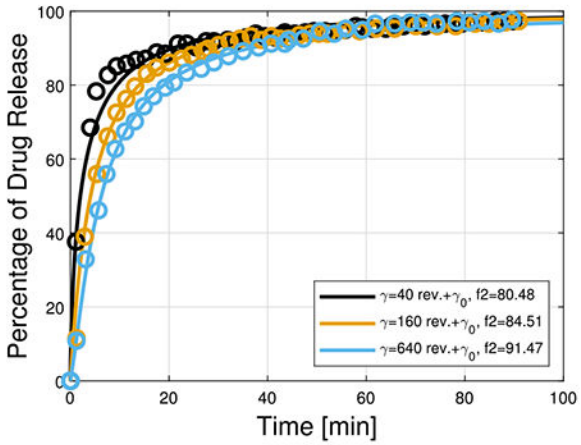

(b)

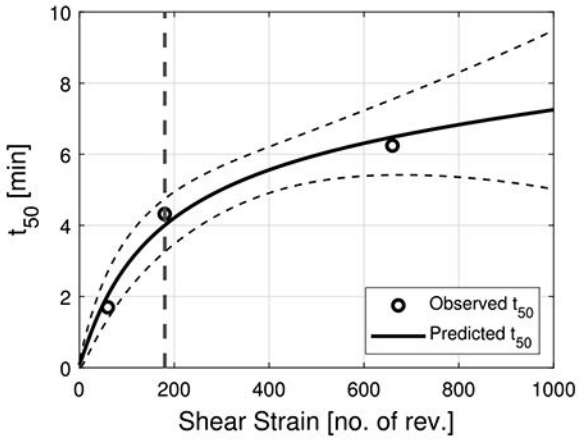

(c)

Fig. 7.

Effect of lubrication on acetaminophen tablets. (a) Model parameters and limiting behavior at full lubrication and no lubrication conditions. The nonlinear multivariate minimization problem additional yields $\gamma_0 = 20$ rev. (b) Predictions of calibrated ROM (solid curves), experimental dissolution data (symbols), and similarity factor f_2 between each set of predicted and measured dissolution profiles. (c) Time to release 50% of the API over a range of lubrication conditions. The vertical dotted line represents the transition of fractional dissolution rate from decreasing to non-monotonic trend with changing total shear strain imparted to the blend. Dashed curves represent the 68% confidence interval.

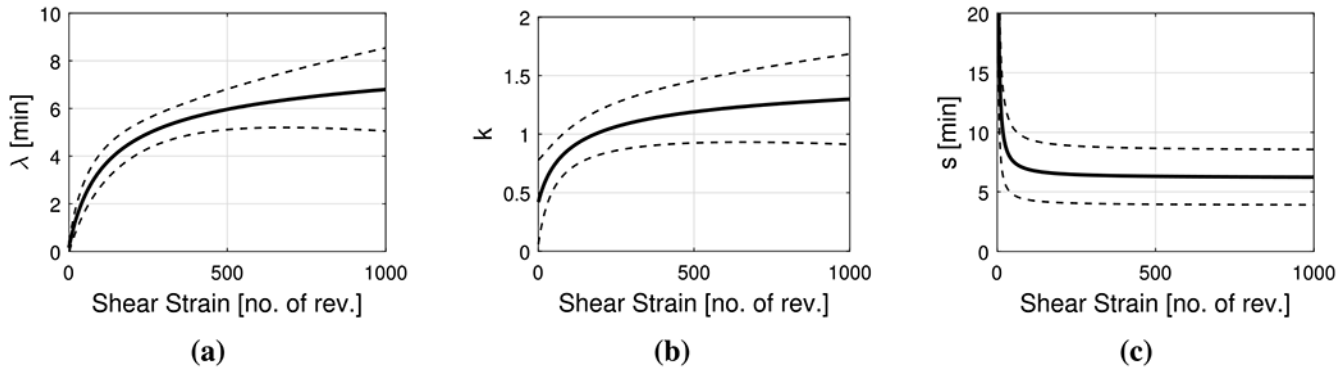

Fig. 8.

Effect of lubrication on acetaminophen tablets. Trend of (a) λ, (b) k, and (c) s. Dashed curves represent the 68% confidence interval.

		Lubrication $\gamma = \bar{\gamma}$
Loose powder blend	$\varepsilon = \varepsilon_c$	$\lambda_{\bar{\gamma}}^{\mathrm{API}} = 0.12$ hr $k_{\bar{\gamma}}^{\mathrm{API}} = 1.35 \times 10^{-5}$ $s_{\bar{\gamma}}^{\mathrm{API}} = 2.63 \times 10^{7}$ hr
Fully compacted powder	$\varepsilon = 0$	$\lambda_{\bar{\gamma}}^{0} = 17.34$ hr $k_{\bar{\gamma}}^{0} = 1.32$ $s_{\bar{\gamma}}^{0} = 8.82$ hr

λ	$e_\lambda = 0.10$
k	$e_k = 5.23$
s	$e_s = 1.59 \times 10^{6}$

(a)

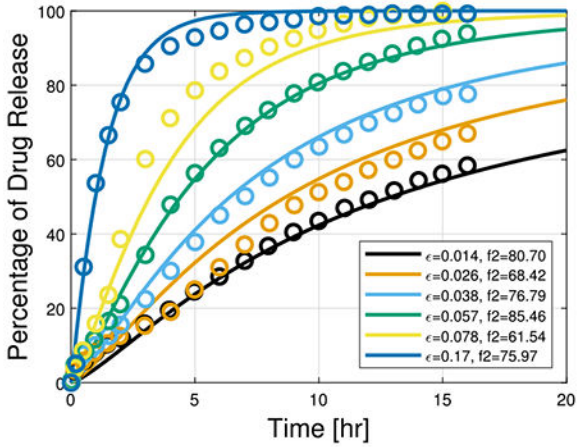

(b)

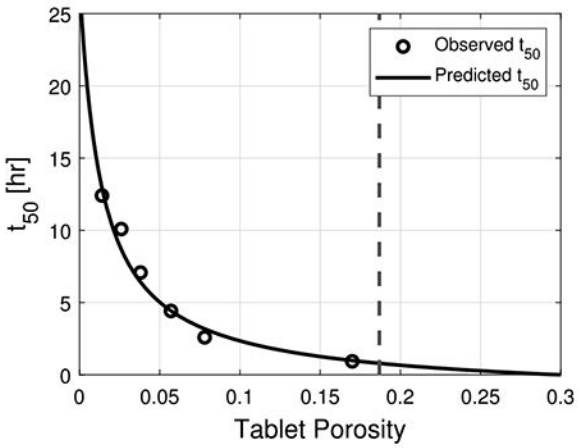

(c)

Fig. 9.

Effect of porosity on amylodextrin tablets. (a) Model parameters and limiting behavior for fully compacted powder and loose powder blend. The nonlinear multivariate minimization problem additional yields $\varepsilon_c = 0.30$. (b) Predictions of calibrated ROM (solid curves), experimental dissolution data (symbols), and similarity factor f_2 between each set of predicted and measured dissolution profiles. (c) Time to release 50% of the API over a range of tablet porosity. The vertical dotted line represents the transition of fractional dissolution rate from non-monotonic to decreasing trend with changing tablet porosity.

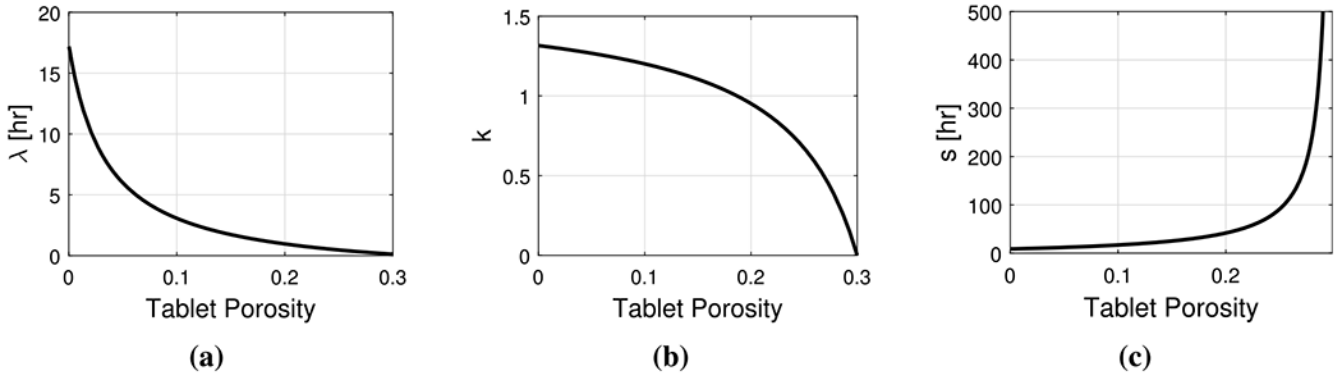

Fig. 10.
Effect of porosity on amylodextrin tablets. Trend of (a) λ, (b) k, and (c) s.

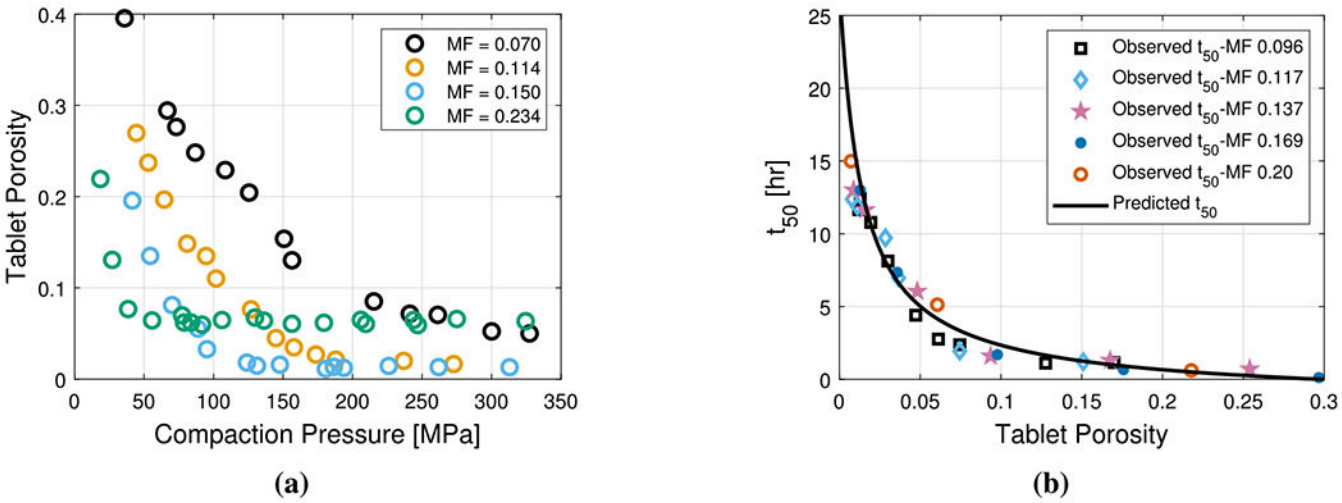

Fig. 11.

Combined effect of porosity and moisture content on amylodextrin tablets (Steendam et al., 2001). (a) Compaction curves using five different moisture fractions. (b) Relationship between time to release 50% of the API (t_{50}) and tablet porosity.

		Lubrication $\gamma = \bar{\gamma}$
Loose powder blend	$\varepsilon = \varepsilon_c$	$\lambda_{\bar{\gamma}}^{\mathrm{API}} = 0.36$ min $k_{\bar{\gamma}}^{\mathrm{API}} = 1.64 \times 10^{-5}$ $s_{\bar{\gamma}}^{\mathrm{API}} = 3.19 \times 10^{8}$ min
Fully compacted powder	$\varepsilon = 0$	$\lambda_{\bar{\gamma}}^{0} = 8.61 \times 10^{6}$ min $k_{\bar{\gamma}}^{0} = 2.35$ $s_{\bar{\gamma}}^{0} = 1.15$ min

λ	$e_\lambda = 6.35 \times 10^{-7}$
k	$e_k = 1.09$
s	$e_s = 4.20 \times 10^{6}$

(a)

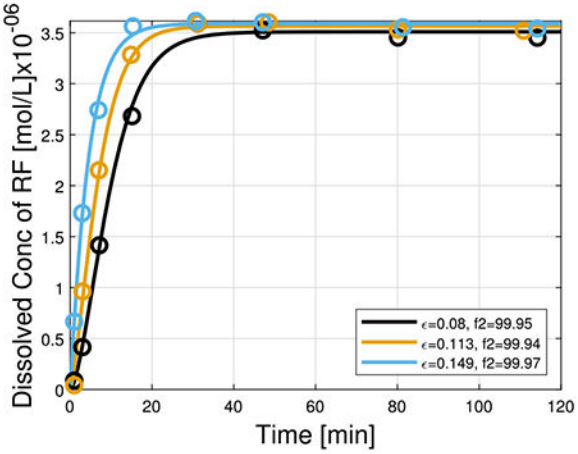

(b)

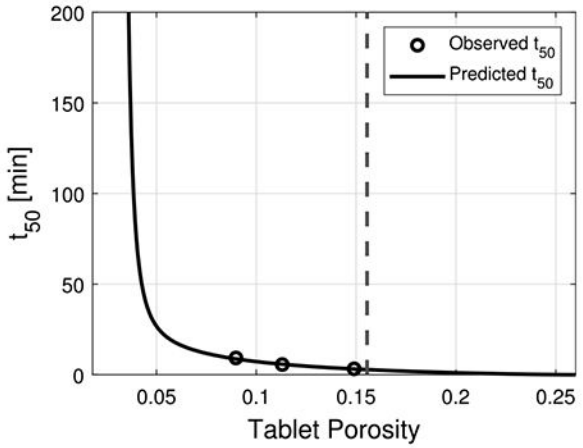

(c)

Fig. 12.

Effect of porosity on riboflavin tablets. (a) Model parameters and limiting behavior for fully compacted powder and loose powder blend. The nonlinear multivariate minimization problem additional yields $\varepsilon_c = 0.26$. (b) Predictions of calibrated ROM (solid curves), experimental dissolution data (symbols), and similarity factor f_2 between each set of predicted and measured dissolution profiles. (c) Time to release 50% of the API over a range of tablet porosity. The vertical dotted line represents the transition of fractional dissolution rate from non-monotonic to decreasing trend with changing tablet porosity.

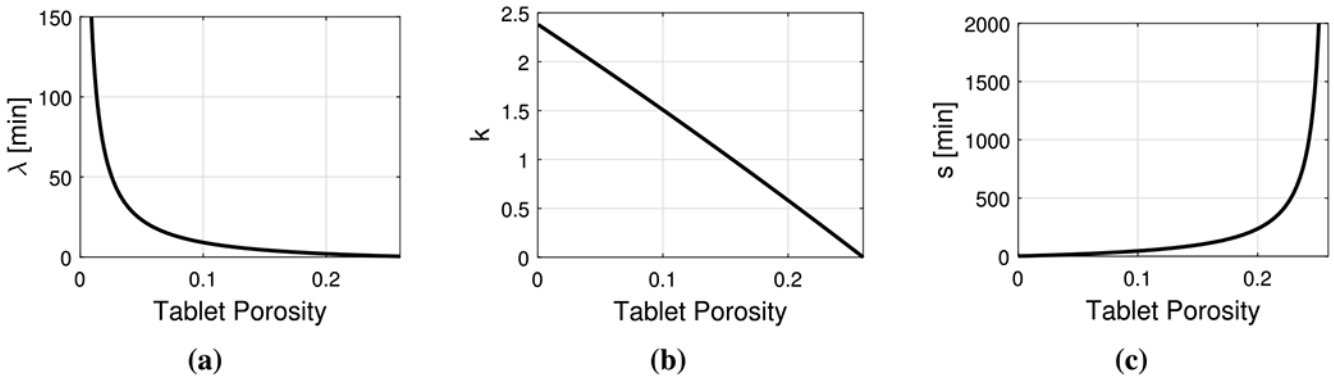

Fig. 13.

Effect of porosity on riboflavin tablets. Trend of (a) λ, (b) k, and (c) s.

		Loose powder blend	Fully compacted powder
		$\varepsilon = \varepsilon_c$ (i.e., $\varepsilon_c/\varepsilon - 1 = 0$)	$\varepsilon = 0$ (i.e., $\varepsilon_c/\varepsilon - 1 \to \infty$)
No lubrication	$\gamma = 0$	$\lambda_0^{\text{API}} = 0.96$ min $k_0^{\text{API}} = 5.46$ $s_0^{\text{API}} = 167.91$ min	$\lambda_0^0 = 59.97$ min $k_0^0 = 1.24$ $s_0^0 = 2.73 \times 10^3$ min
Full lubrication	$\gamma \to \infty$	$\lambda_\infty^{\text{API}} = 141.37$ min $k_\infty^{\text{API}} = 0.99$ $s_\infty^{\text{API}} = 550.78$ min	$\lambda_\infty^0 = 125.31$ min $k_\infty^0 = 2.34$ $s_\infty^0 = 2.76 \times 10^3$ min

λ	$a_\lambda = 0.002$ rev^{-1} $b_\lambda = 8.04 \times 10^{-5}$ rev^{-1} $c_\lambda = 0.78$
k	$a_k = 2.85 \times 10^7$ rev^{-1} $b_k = 7.58 \times 10^7$ rev^{-1} $c_k = 5.61 \times 10^7$
s	$a_s = 4.55 \times 10^4$ rev^{-1} $b_s = 3.65 \times 10^4$ rev^{-1} $c_s = 1.71 \times 10^5$

(a)

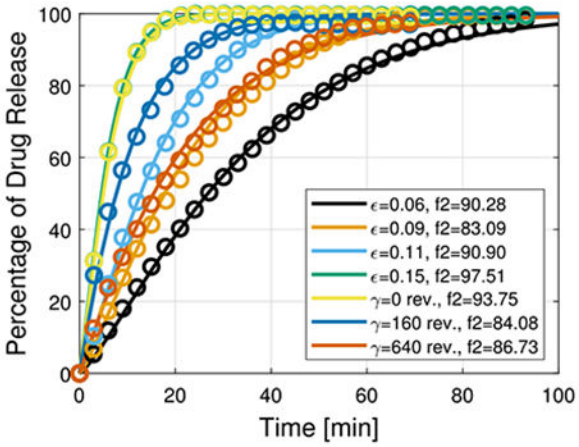

(b)

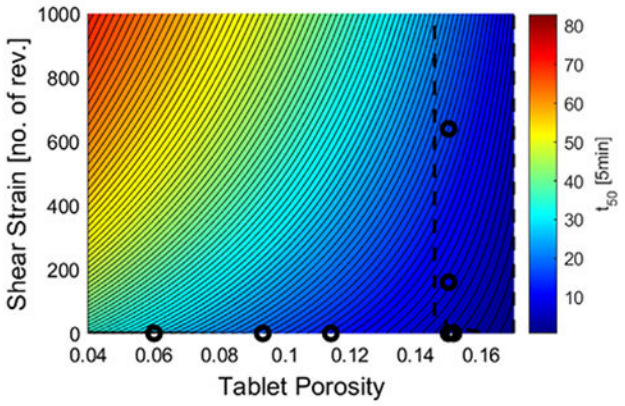

(c)

Fig. 14.

Effect of lubrication and porosity on acetaminophen tablets. (a) Model parameters and limiting behavior for fully compacted powder, loose powder blend, at full lubrication and no lubrication condition. (b) Predictions of calibrated ROM (solid curves), experimental dissolution data (symbols), and similarity factor f_2 between each set of predicted and measured dissolution profiles. (c) Time to release 50% of the API over a range of tablet porosity and lubrication conditions. The first dotted curve represents the transition of fractional dissolution rate from increasing to non-monotonic trend with changing tablet porosity and shear and the second dotted line represents decreasing fractional dissolution rate at critical porosity and any shear.

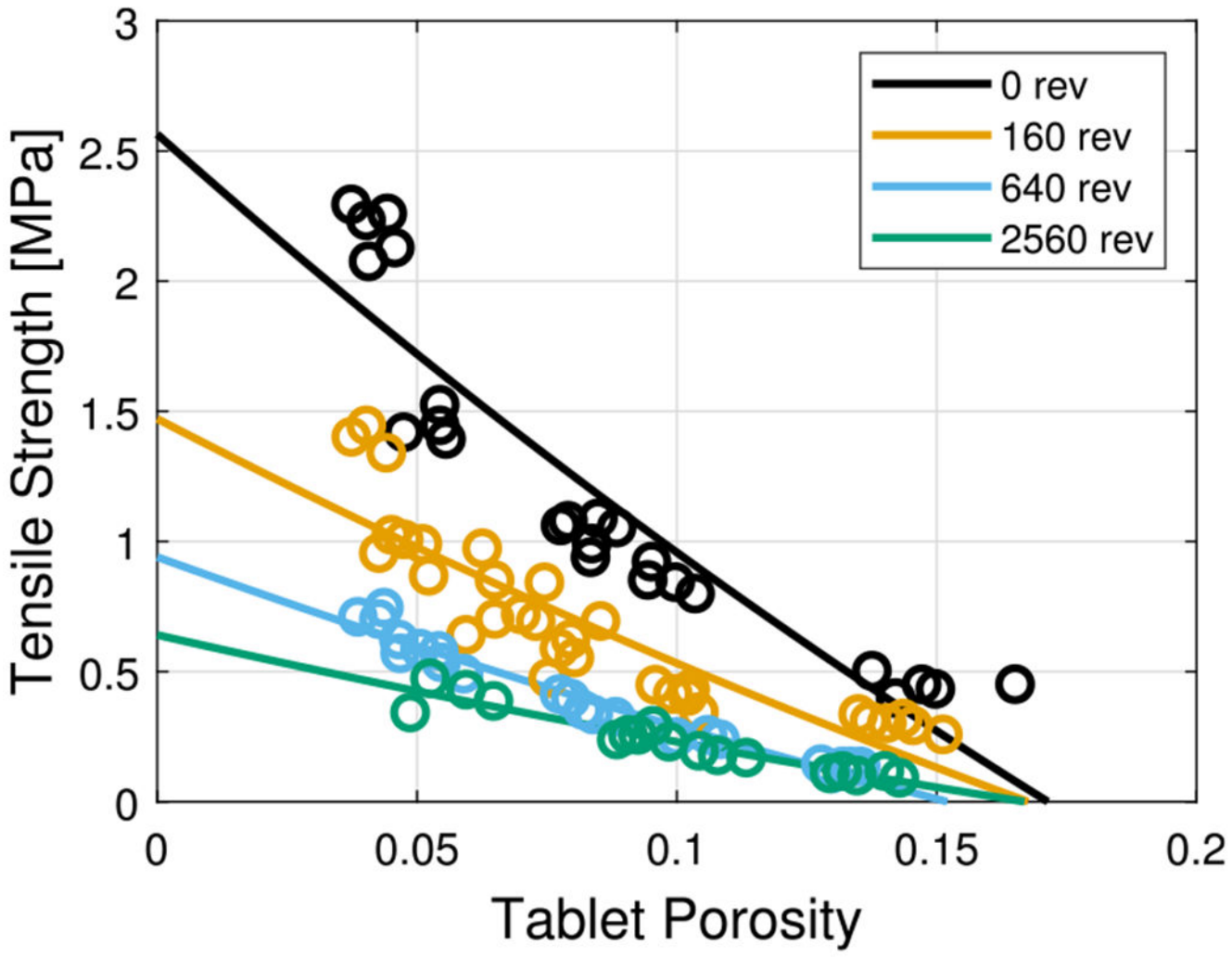

Fig. 15.

Tensile strength as a function of tablet porosity, circles represent experimental data and lines represent model prediction. The tensile strength was affected by both compaction force and shear strain.

		Lubrication $\gamma = \bar{\gamma}$
Loose powder blend	$\varepsilon = \varepsilon_c$	$\lambda_{\bar{\gamma}}^{\mathrm{API}} = 10.04$ min $k_{\bar{\gamma}}^{\mathrm{API}} = 1.06$ $s_{\bar{\gamma}}^{\mathrm{API}} = 3.61$ min
Fully compacted powder	$\varepsilon = 0$	$\lambda_{\bar{\gamma}}^{0} = 27.48$ min $k_{\bar{\gamma}}^{0} = 1.94$ $s_{\bar{\gamma}}^{0} = 12.47$ min

λ	$e_\lambda = 0.14$
k	$e_k = 0.62$
s	$e_s = 2.20$

(a)

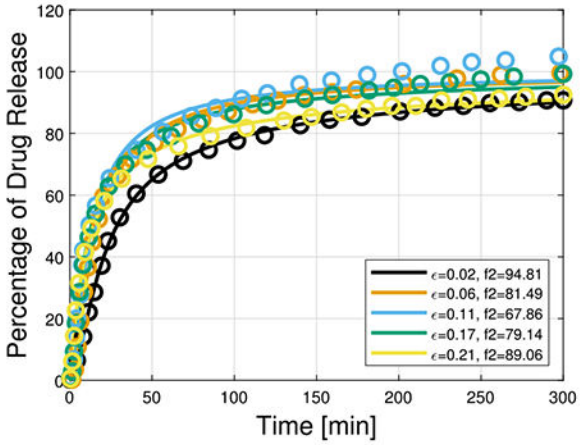

(b)

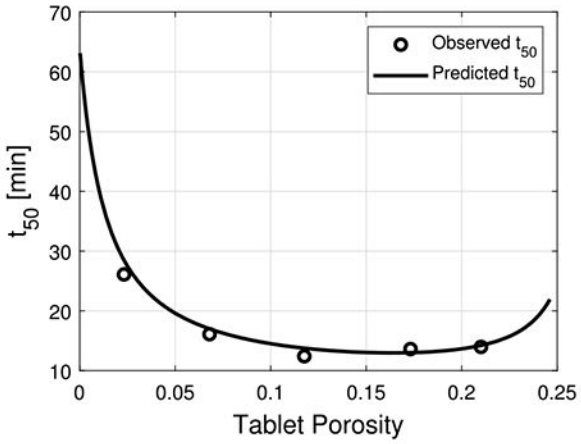

(c)

Fig. 16.

Effect of porosity on indomethacin tablets. (a) Model parameters and limiting behavior for fully compacted powder and loose powder blend. The nonlinear multivariate minimization problem additional yields $\varepsilon_c = 0.25$. (b) Predictions of calibrated ROM (solid curves), experimental dissolution data (symbols), and similarity factor f_2 between each set of predicted and measured dissolution profiles. (c) Time to release 50% of the API over a range of tablet porosity. The fractional dissolution rate is non-monotonic for any tablet porosity.

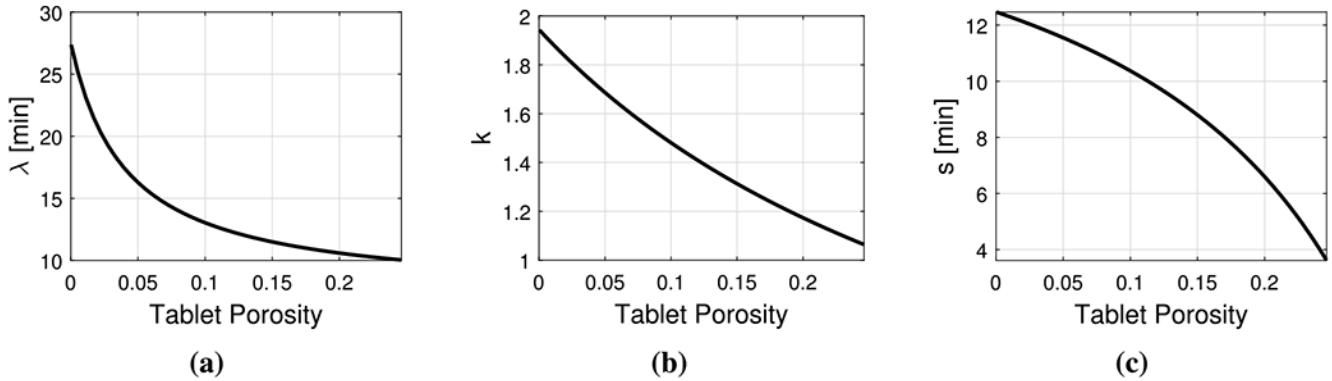

Fig. 17.

Effect of porosity on indomethacin tablets. Trend of (a) λ, (b) k, and (c) s.

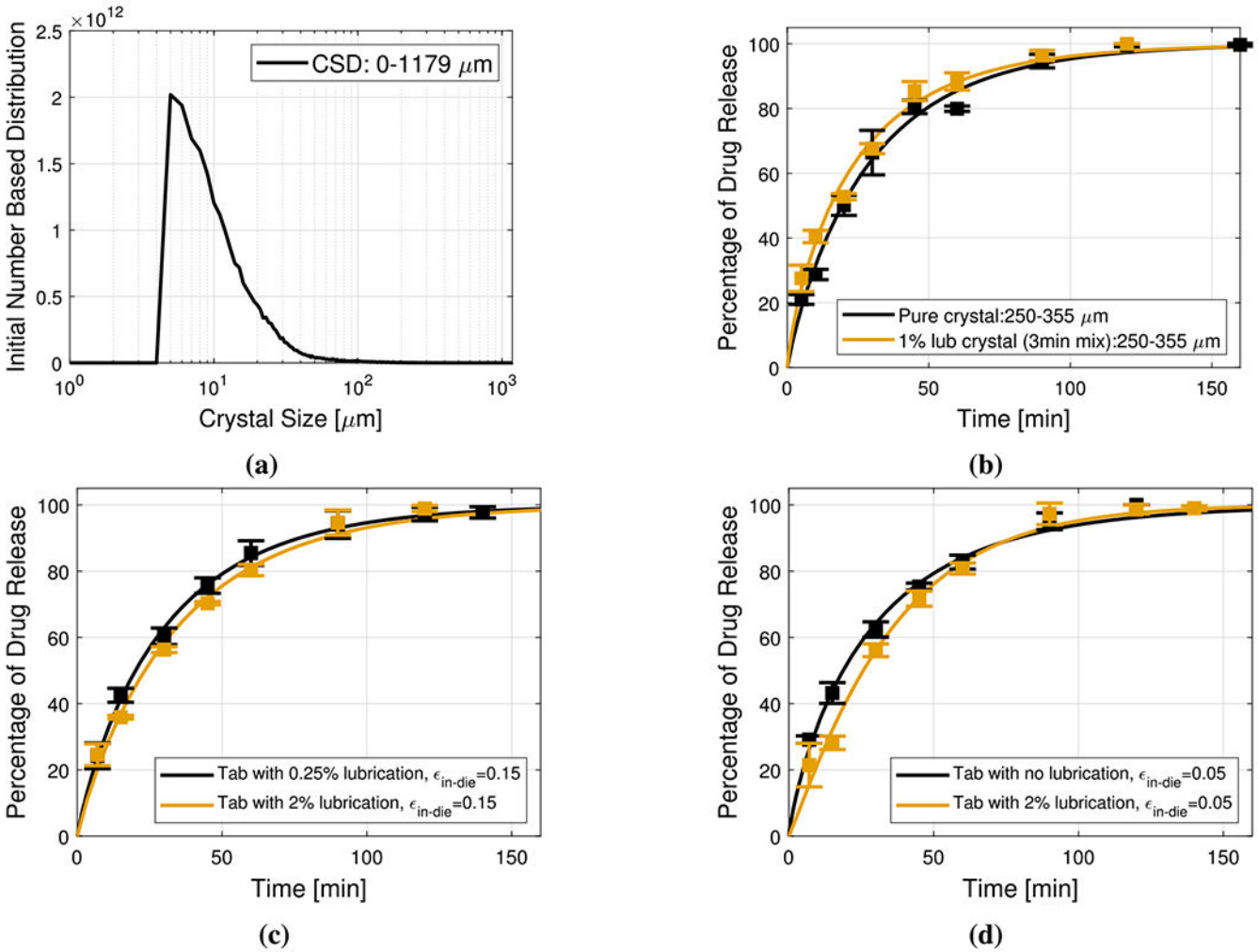

Fig. 18.

Lubrication effects in lomustine crystals. (a) Lomustine crystal size distribution. (b) Lubricated and unlubricated loose crystals show similar dissolution profile. (c) Lomustne tablets of 0.25% lubrication and 2% lubrication show similar dissolution profile. (d) Lomustne tablets of no lubrication and 2% lubrication show similar dissolution profile.

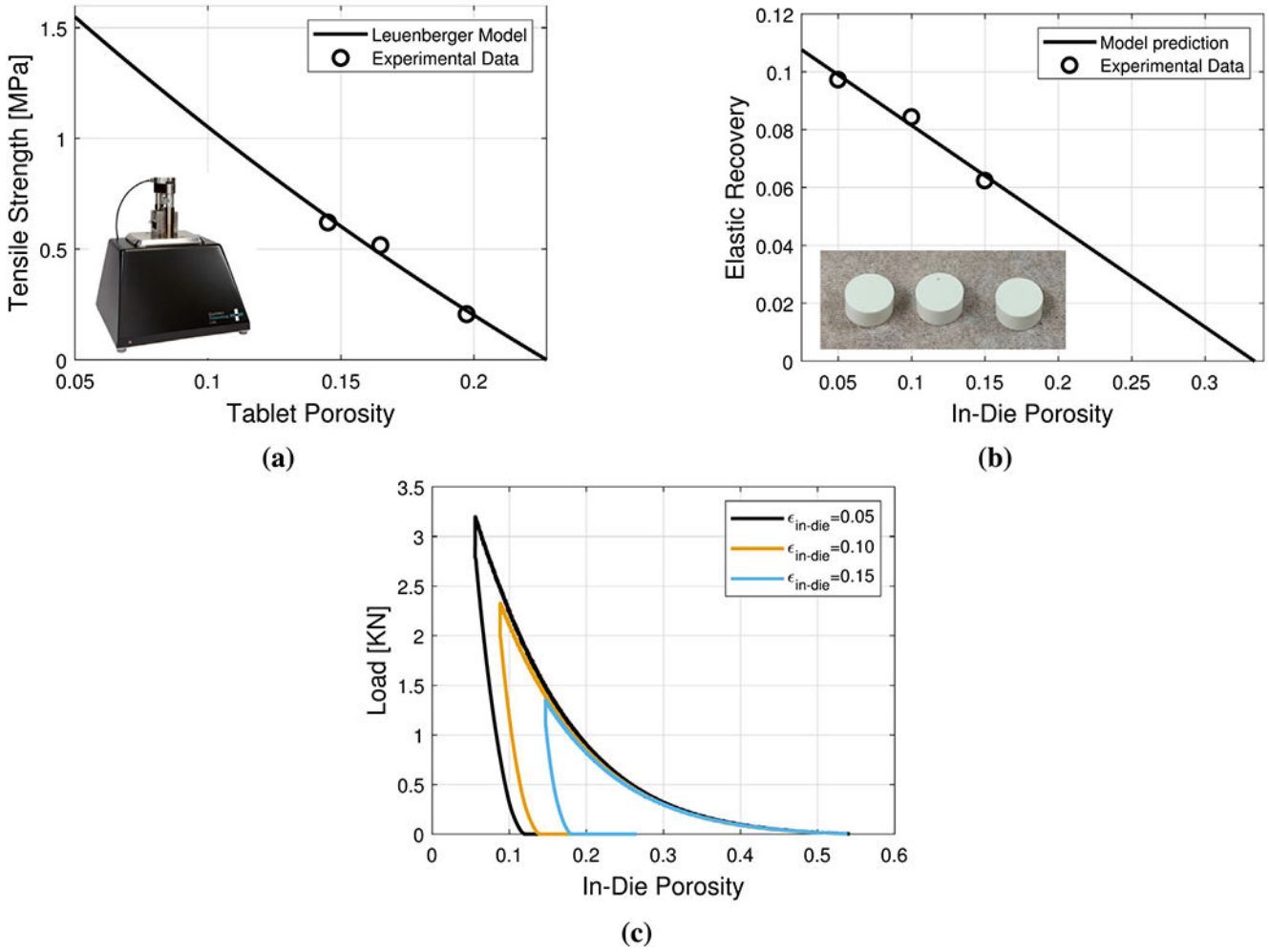

Fig. 19.

Lomustine tablets fabricated in a Gamlen D Series bench-top compaction simulator. (a) Tensile strength as a function of tablet porosity. (b) Elastic recovery as a function of in-die tablet porosity. (c) Compaction plots.

		Lubrication $\gamma = \bar{\gamma}$
Loose powder blend	$\varepsilon = \varepsilon_c$	$\lambda_{\bar{\gamma}}^{\mathrm{API}} = 26.13$ min $k_{\bar{\gamma}}^{\mathrm{API}} = 1.04$ $s_{\bar{\gamma}}^{\mathrm{API}} = 7.96 \times 10^6$ min
Fully compacted powder	$\varepsilon = 0$	$\lambda_{\bar{\gamma}}^{0} = 6.77 \times 10^4$ min $k_{\bar{\gamma}}^{0} = 1.46$ $s_{\bar{\gamma}}^{0} = 82.59$ min

λ	$e_\lambda = 3.07 \times 10^{-4}$
k	$e_k = 3.67$
s	$e_s = 2.99 \times 10^4$

(a)

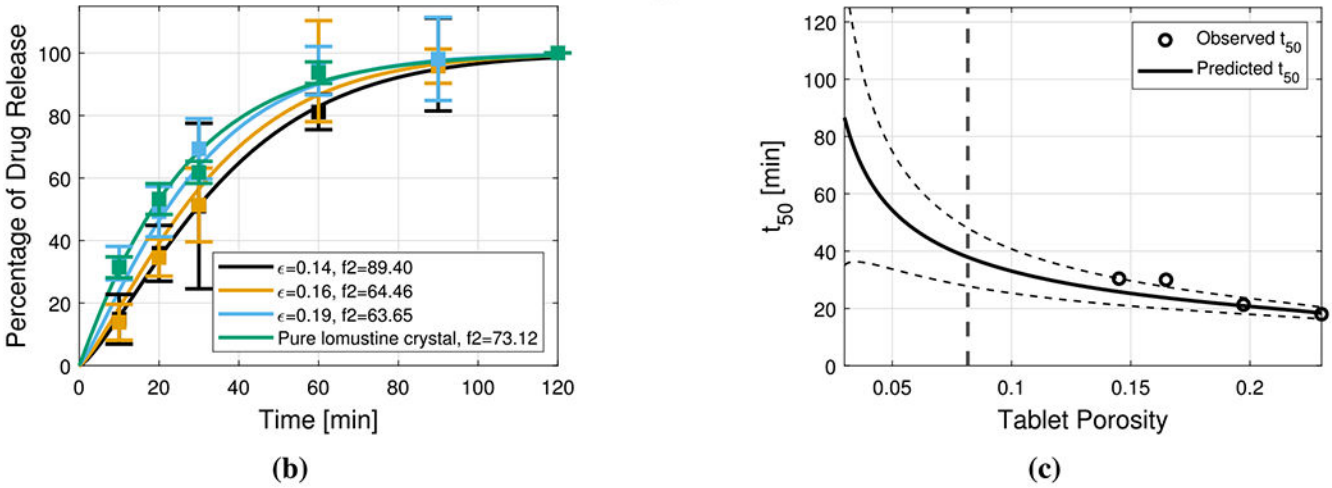

(b) (c)

Fig. 20.

Effect of porosity on lomustine tablets. (a) Model parameters and limiting behavior for fully compacted powder and loose powder blend. The critical porosity ($\varepsilon_c = 0.23$) used for this nonlinear multivariate minimization problem was obtained from the Leuenberger model (Eq. (29)) fitting. (b) Predictions of calibrated ROM (solid curves), experimental dissolution data (symbols), and similarity factor f_2 between each set of predicted and measured dissolution profiles. (c) Time to release 50% of the API over a range of tablet porosity. The vertical dotted line represents the transition of fractional dissolution rate from non-monotonic to increasing trend with changing tablet porosity. Dashed curves represent the 68% confidence interval.

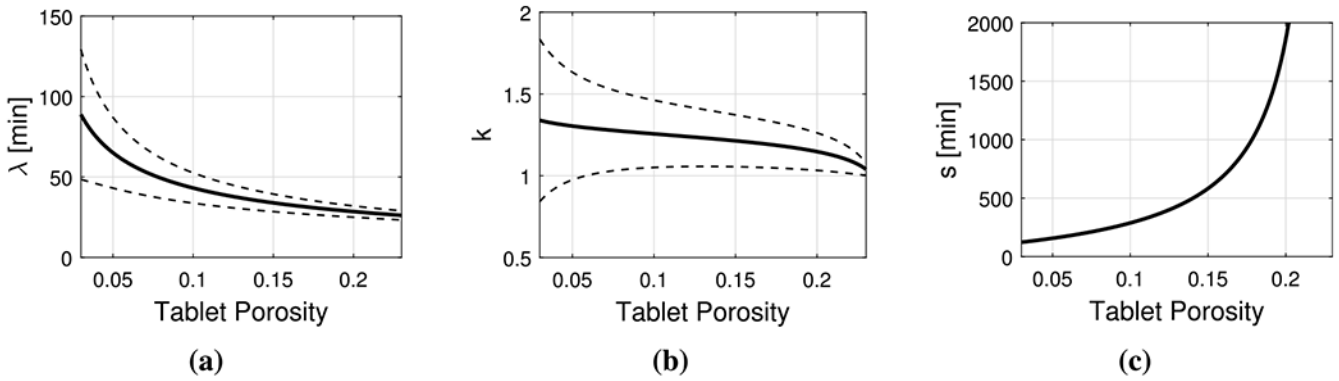

Fig. 21.

Effect of porosity on lomustine tablets. Trend of (a) λ, (b) k, and (c) s. Dashed curves represent the 68% confidence interval.

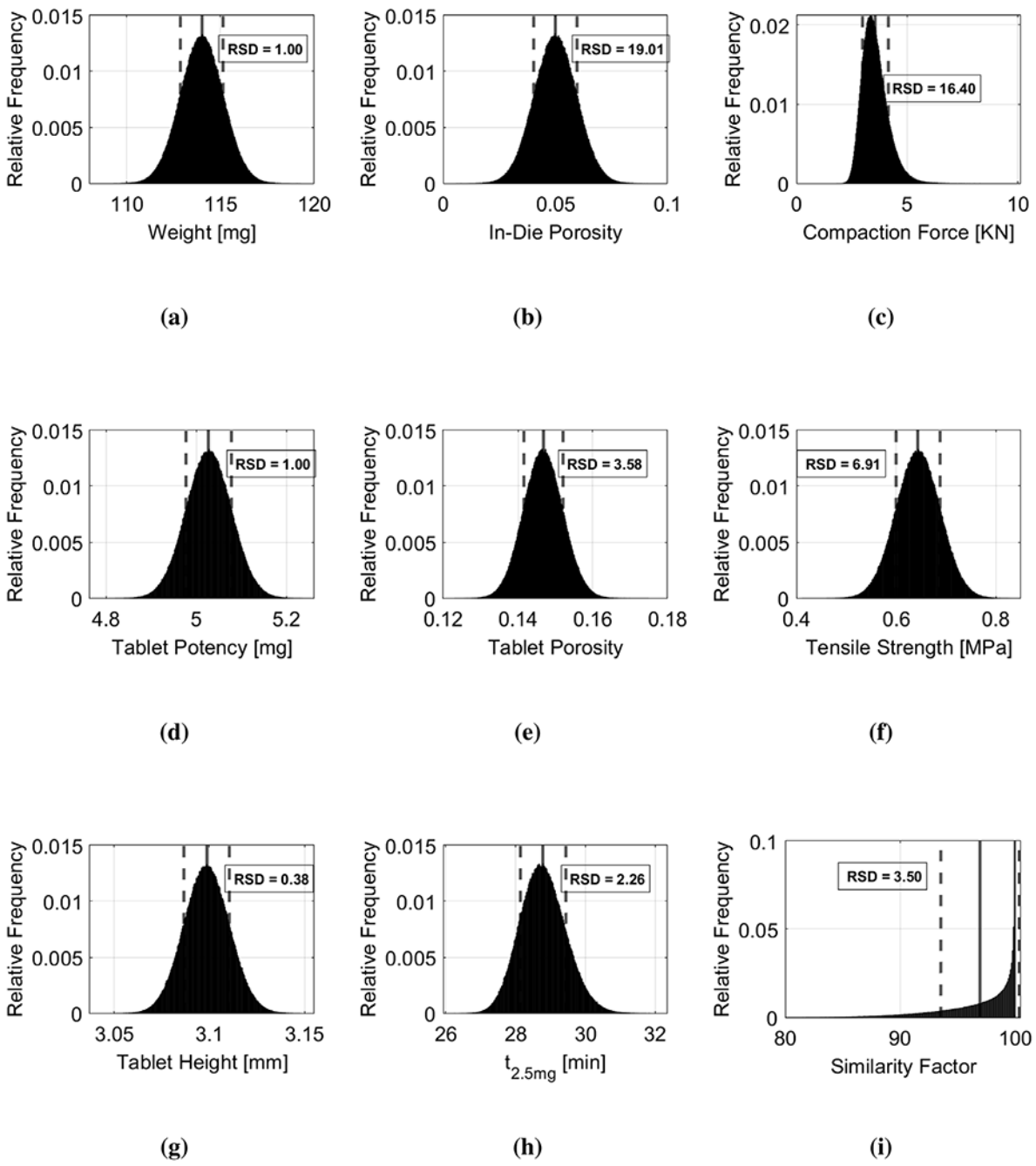

Fig. 22.

Impact of weight variability on CQAs of lomustine tablets under an idealized state of control of the tableting process where the punch separation at peak force is kept constant. Relative frequency distribution of (a) weight, (b) in-die porosity, (c) compaction force, (d) tablet potency, (e) tablet porosity, (f) tensile strength, (g) tablet height, (h) time to release half of the target product dosage, and (i) similarity factor with respect to the target product profile. Vertical lines represent the mean value and standard deviation bounds, with RSD being the relative standard deviation.

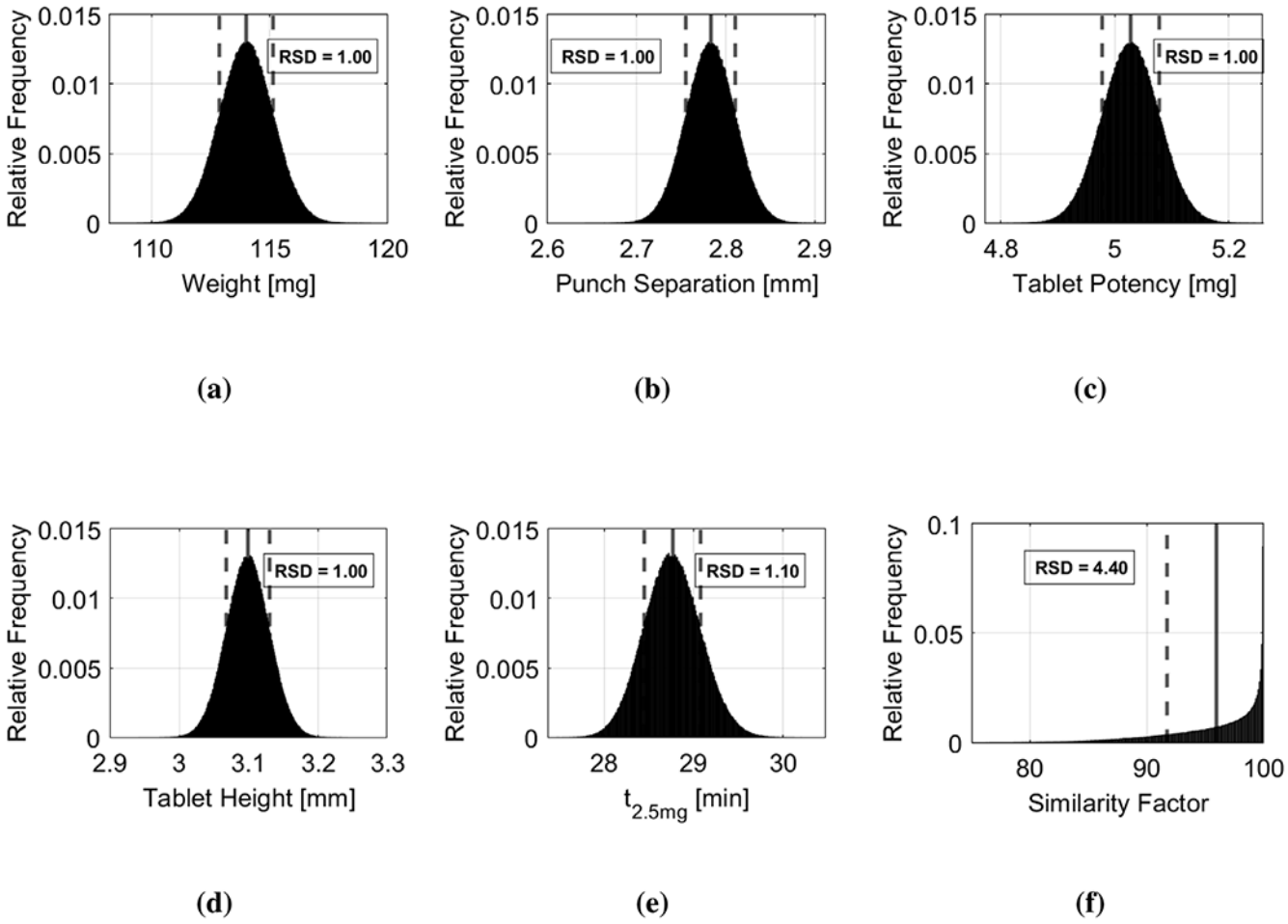

Fig. 23.

Impact of weight variability on CQAs of lomustine tablets under an idealized state of control of the tableting process where the compaction force is kept constant. Relative frequency distribution of (a) weight, (d) punch separation at peak force, (d) tablet height, (c) potency, (e) time to release half of the target product dosage, and (f) similarity factor with respect to the target product profile. Vertical lines represent the mean value and standard deviation bounds, with RSD being the relative standard deviation.

Table 1

Comparison of the generalized Weibull dissolution model to other dissolution models.

Fraction of drug released $M(t)/M_\infty$	Eq.	Type	Model equivalence			
			λ	k	s	# order
$1-\mathrm{e}^{-(t/\lambda)^k}$	(3)	IFR and DFR	λ	k	∞	exact
$1-(1-t/a)^n$	(6)	IFR	a/n	1	$-a$	exact
$C_1t^m+C_2t^2m$	(10)	DFR and NMFR	$C_1^{-1/m}$	m	$\left[-C_1/\left(C_1^2+2C_2\right)\right]^{1/m}$	two terms

Table 2

Generalized Weibull dissolution model parameters.

Case no.	Model	λ	k	s	SSE	R-squared	Akaike information Criterion (AIC)	Ref. No.	Formulation	No of data points (n)	Fractional rate type
1	Weibull Model	25.16	1.43		17.38	0.999	Ref (AIC-0)	Hernandez et al. (2016)	9% APAP, 90% Lactose, 1% MgSt (Strain 0 rev.)	35	IFR
	generalized Weibull	25.16	1.43	1.62E+06	17.38	0.999	2.00				
2	Weibull Model	27.96	1.36		69.68	0.998	Ref (AIC-0)	Hernandez et al. (2016)	9% APAP, 90% Lactose, 1% MgSt (Strain 160 rev.)	39	IFR
	generalized Weibull	28.03	1.36	1.10E+06	69.68	0.998	2.00				
3	Weibull Model	48.05	1.36		363.45	0.989	Ref (AIC-0)	Hernandez et al. (2016)	9% APAP, 90% Lactose, 1% MgSt (Strain 640 rev.)	40	IFR
	generalized Weibull	48.01	1.36	1.64E+06	363.45	0.989	2.00				
4	Weibull Model	73.38	1.06		184.31	0.991	Ref (AIC-0)	Hernandez et al. (2016)	9% APAP, 90% Lactose, 1% MgSt (Strain 2560 rev.)	40	IFR
	generalized Weibull	73.42	1.06	6.30E+08	184.31	0.991	2.00				
5	Weibull Model	7.59	1.55		0.001	0.999	Ref (AIC-0)	Dokoumetzidis et al. (2006)	Metoprolol tartrate tablet (Fast Dissolution)	8	IFR
	generalized Weibull	7.59	1.55	3.57E+07	0.001	0.999	2.20				
6	Weibull Model	15.25	1.49		0.002	0.998	Ref (AIC-0)	Dokoumetzidis et al. (2006)	Metoprolol tartrate tablet (Medium Dissolution)	8	IFR
	generalized Weibull	15.24	1.49	8.05E+05	0.002	0.998	1.90				
7	Weibull Model	36.18	1.12		0.005	0.996	Ref (AIC-0)	Dokoumetzidis et al. (2006)	Metoprolol tartrate tablet (Slow Dissolution)	11	IFR
	generalized Weibull	36.09	1.13	1.92E+08	0.005	0.996	1.93				
8	Weibull Model	265.83	1.23		204.37	0.994	Ref (AIC-0)	Weiss (1996)	Extended Release Formulation	29	NMFR
	generalized Weibull	191.71	1.81	210.9	37.69	0.999	−47.02				
9	Weibull Model	2.92	0.41		304.17	0.929	Ref (AIC-0)	Pingali et al. (2011)	9% APAP, 45% Lactose (Pharmatose),	45	NMFR
	generalized Weibull	1.12	2.01	0.65	35.51	0.992	−94.65		45% MCC (Avicel 102), 1% MgSt (Strain 40 rev.)		

Case no.	Model	λ	k	s	SSE	R-squared	Akaike information Criterion (AIC)	Ref. No.	Formulation	No of data points (n)	Fractional rate type
10	Weibull Model	7.74	0.66		438.65	0.960	Ref (AIC-0)	Pingali et al. (2011)	9% APAP, 45% Lactose (Pharmatose),	37	NMFR
	generalized Weibull	3.57	1.73	2.52	17.87	0.998	−116.42		45% MCC (Avicel 102), 1% MgSt (Strain 160 (rev.)		
11	Weibull Model	10.58	0.70		158.92	0.988	Ref (AIC-0)	Pingali et al. (2011)	9% APAP, 45% Lactose (Pharmatose),	35	NMFR
	generalized Weibull	6.91	1.08	9.44	37.95	0.997	−48.12		45% MCC (Avicel 102), 1% MgSt (Strain 640 rev.)		

Table 3

Generalized Weibull dissolution model parameters for atorvastatin tablets.

Case no.	Model Parameter	λ	k	s	SSE	R-squared	Akaike information Criterion (AIC)	Ref. No.	Formulation	No of data points (n)	Fractional rate type
1	Weibull Model	35.43	0.6		96.39	0.972	Ref (AIC-0)	Prihapsara (2020)	Atorvastatin Innovator, (pH 1.2 buffer)	6	NMFR
	generalized Weibull	3.34	19.32	2.73	9.94	0.997	−11.63				
2	Weibull Model	21.39	0.75		401.87	0.927	Ref (AIC-0)	Prihapsara (2020)	Atorvastatin Branded, (pH 1.2 buffer)	6	NMFR
	generalized Weibull	4.09	42.71	3.71	66.3	0.988	−8.81				
3	Weibull Model	33.54	0.59		32.51	0.991	Ref (AIC-0)	Prihapsara (2020)	Atorvastatin Generic, (pH 1.2 buffer)	6	NMFR
	generalized Weibull	5.98	2.31	2.79	1.97	0.999	−14.81				
4	Weibull Model	7.69	0.82		77.19	0.954	Ref (AIC-0)	Prihapsara (2020)	Atorvastatin Innovator, (pH 4.5 buffer)	6	NMFR
	generalized Weibull	3.24	22.54	2.84	5.36	0.997	−14.01				
5	Weibull Model	3.69	0.53		9.84	0.984	Ref (AIC-0)	Prihapsara (2020)	Atorvastatin Branded, (pH 4.5 buffer)	6	DFR
	generalized Weibull	3.69	0.53	3.10e+05	9.84	0.984	2.00				
6	Weibull Model	94.99	0.97		17.29	0.98	Ref (AIC-0)	Prihapsara (2020)	Atorvastatin Generic, (pH 4.5 buffer)	6	NMFR
	generalized Weibull	29.45	1.79	11.34	9.5034	0.989	−1.59				
7	Weibull Model	7.44	0.39		43.55	0.992	Ref (AIC-0)	Prihapsara (2020)	Atorvastatin Innovator, (pH 6.8 buffer)	6	NMFR
	generalized Weibull	1.51	9.99	1.12	12.94	0.998	−5.28				
8	Weibull Model	4.45	0.29		17.34	0.997	Ref (AIC-0)	Prihapsara (2020)	Atorvastatin Branded, (pH 6.8 buffer)	6	NMFR
	generalized Weibull	0.68	6.63	0.45	6.7998	0.999	−3.62				
9	Weibull Model	19.38	1.33		13.86	0.998	Ref (AIC-0)	Prihapsara (2020)	Atorvastatin Generic, (pH 6.8 buffer)	6	NMFR
	generalized Weibull	17.83	1.46	54.63	10.91	0.999	0.56				

Table 4

Limiting behavior of the reduced order model of pharmaceutical tablet dissolution for continuous manufacturing.

		Loose powder blend	**Fully compacted powder**
		$\varepsilon = \varepsilon_c$ **(i.e.,** $\varepsilon_c/\varepsilon - 1 = 0$**)**	$\varepsilon = 0$ **(i.e.,** $\varepsilon_c/\varepsilon - 1 \to \infty$**))**
No lubrication	$\gamma = 0$	λ_0^{API} k_0^{API} s_0^{API}	λ_0^0 k_0^0 s_0^0
Full lubrication	$\gamma \to \infty$	$\lambda_\infty^{\mathrm{API}}$ k_∞^{API} s_∞^{API}	λ_∞^0 k_∞^0 s_∞^0

Table 5

Dissolution specifications for lomustine tablets.

Medium	0.05 M phosphate buffer, 1% sodium lauryl sulfate (surfactant)
pH	6.8
Media volume	900 mL
USP apparatus	II
Paddle speed	75 rpm
Quantitative procedure	UV (231 nm)